The Astrophysical Journal, 958:62 (19pp), 2023 November 20 https://doi.org/10.3847/1538-4357/acfaeb
© 2023. The Author(s). Published by the American Astronomical Society.
OPEN ACCESS

Identification of Superclusters and Their Properties in the Sloan Digital Sky Survey Using the WHL Cluster Catalog

Shishir Sankhyayan[1], Joydeep Bagchi[2], Elmo Tempel[1,3], Surhud More[4,5], Maret Einasto[1], Pratik Dabhade[6,7], Somak Raychaudhury[4,8], Ramana Athreya[9], and Pekka Heinämäki[10]
[1] Tartu Observatory, University of Tartu, Observatooriumi 1, 61602 Tõravere, Estonia; shishir.sankhyayan@ut.ee, shishir9898@gmail.com
[2] Department of Physics and Electronics, CHRIST (Deemed to be University), Bengaluru-560029, India
[3] Estonian Academy of Sciences, Kohtu 6, 10130 Tallinn, Estonia
[4] The Inter-University Centre for Astronomy and Astrophysics (IUCAA), S.P. Pune University Campus, Post Bag 4, Pune 411007, India
[5] Kavli Institute for the Physics and Mathematics of the Universe (IPMU), 5-1-5 Kashiwanoha, Kashiwashi, Chiba 277-8583, Japan
[6] Instituto de Astrofísica de Canarias, Calle Vía Láctea, s/n, E-38205, La Laguna, Tenerife, Spain
[7] Universidad de La Laguna (ULL), Departamento de Astrofisica, E-38206, Tenerife, Spain
[8] Department of Physics, Ashoka University, Sonipat, Haryana 131029, India
[9] Indian Institute of Science Education and Research (IISER), Dr. Homi Bhabha Road, Pashan, Pune 411008, India
[10] Tuorla Observatory, Department of Physics and Astronomy, University of Turku, Vesilinnantie 5, 20014 Turku, Finland
Received 2022 December 13; revised 2023 September 11; accepted 2023 September 11; published 2023 November 13

Abstract

Superclusters are the largest massive structures in the cosmic web, on tens to hundreds of megaparsec scales. They are the largest assembly of galaxy clusters in the Universe. Apart from a few detailed studies of such structures, their evolutionary mechanism is still an open question. In order to address and answer the relevant questions, a statistically significant, large catalog of superclusters covering a wide range of redshifts and sky areas is essential. Here, we present a large catalog of 662 superclusters identified using a modified friends-of-friends algorithm applied on the WHL (Wen–Han–Liu) cluster catalog within a redshift range of $0.05 \leqslant z \leqslant 0.42$. We name the most massive supercluster at $z \sim 0.25$ as the *Einasto Supercluster*. We find that the median mass of superclusters is $\sim 5.8 \times 10^{15}\ M_{\odot}$ and the median size $\sim$65 Mpc. We find that the supercluster environment slightly affects the growth of clusters. We compare the properties of the observed superclusters with the mock superclusters extracted from the Horizon Run 4 cosmological simulation. The properties of the superclusters in the mocks and observations are in broad agreement. We find that the density contrast of a supercluster is correlated with its maximum extent with a power-law index, $\alpha \sim -2$. The phase-space distribution of mock superclusters shows that, on average, $\sim$90% of part of a supercluster has a gravitational influence on its constituents. We also show the mock halos' average number density and peculiar velocity profiles in and around the superclusters.

Unified Astronomy Thesaurus concepts: Superclusters (1657); Galaxy clusters (584); Catalogs (205); Large-scale structure of the universe (902)

Supporting material: machine-readable tables

1. Introduction

The intricate network of the distribution of galaxies and matter in the Universe is called the cosmic web (Bond et al. 1996). The details of the cosmic web help in our understanding of the cosmological models governing the evolution of structures in the Universe. The main components of the cosmic web are clusters, two-dimensional walls, one-dimensional filaments, and underdense regions called voids.

In the cosmic web, there exist large coherent regions ($\sim$10–100 Mpc) that are larger than the dimensions of galaxy clusters, which span about a few megaparsecs. Moreover, these regions are extremely massive and contain several groups and clusters of galaxies apart from the galaxies and intergalactic dark and baryonic matter in between the clusters. Cumulatively, these regions are called superclusters. Superclusters are not as abundant as galaxies or even groups and clusters, but they are known to affect the evolution of the galaxies within them (e.g., Einasto et al. 2007b, 2011c, 2014; Lietzen & Einasto 2016). It is still an open question as to how these giant structures form and evolve in the cosmic web, and answering it requires detailed studies involving observations and simulations. Although this is a growing field of research, which is getting enriched with the availability of more data, a single widely accepted definition of a supercluster does not exist as yet. Superclusters are coherent regions in the cosmic web that have been defined in different ways in the literature. The two extreme definitions of a supercluster are based on the largest bound structures in the Universe and the largest regions with converging peculiar velocity field flows. The superclusters in the literature can be broadly divided into three categories: (1) the gravitationally bound regions; (2) the unbound overdense regions in the Universe; and (3) the converging peculiar velocity field regions. According to definition (1), they have been defined as the largest overdense regions, with sufficiently high matter density to overcome the global expansion of the Universe. They would eventually collapse and form gravitationally bound systems (Dünner et al. 2006; Araya-Melo et al. 2009; Luparello et al. 2011; Chon et al. 2015). According to definition (3), using the peculiar velocity field, they have been defined as regions in which, on average, the peculiar velocities of galaxies converge (Tully et al. 2014; Pomarède et al. 2015; Dupuy et al. 2019; Pomarède et al. 2020). These superclusters form regions of

Original content from this work may be used under the terms of the Creative Commons Attribution 4.0 licence. Any further distribution of this work must maintain attribution to the author(s) and the title of the work, journal citation and DOI.

dynamical influence where they act as great attractors that grow by the inflow of matter from lower-density regions (Tully et al. 2014). Einasto et al. (2019) and Dupuy et al. (2019) showed that the whole cosmic web can be divided into regions of dynamical influence or the basins of attraction. This means that type (3) superclusters contain some parts of the underdense void regions surrounding them. Observationally, Laniakea—our home supercluster (Tully et al. 2014)—has been identified using the rich observational data of the peculiar velocities of the nearby galaxies. But such data are still not available for distant galaxies; therefore, the velocity field flow method of estimating regions of convergence cannot be derived for them. However, these converging peculiar velocity field regions (or the "basins of attraction") can be identified in simulations. It is often seen that the supercluster definition (1) of gravitationally bound systems picks up the central regions of superclusters defined with other criteria (definitions (2) and (3)), for example, overdensities in the luminosity density field (e.g., Einasto et al. 2022). Definition (2) picks up the overdensities present in the matter density field. These regions do not contain any parts of underdense void regions. The overdensity threshold to consider in defining these types of superclusters is not set, and depending on the focus of the study, it varies in the literature (see for example, Einasto et al. 2007a; Liivamägi et al. 2012; Lietzen et al. 2016; Einasto et al. 2019).

Superclusters are traditionally identified using the friends-of-friends (FoF) algorithm. FoF is also used to find bound halos in simulations (Knebe et al. 2011). FoF has been used in several supercluster-finding works (e.g., Einasto et al. 1997; Chow-Martínez et al. 2014; Bagchi et al. 2017) in various forms, using clusters as well as galaxies as their input data. Apart from FoF, there are other methods as well to extract superclusters. For example, by applying different density threshold cuts on the luminosity density field of the galaxy distribution (Einasto et al. 2007a; Liivamägi et al. 2012; Lietzen et al. 2016) and the watershed method, by applying it on the number density field constructed by Voronoi tessellation (Neyrinck 2008; Nadathur & Crittenden 2016).

Recent studies show that a supercluster's size, mass, and luminosity show some evolution with redshift. In this context, luminosity represents the total luminosity of all galaxies within the supercluster. Size refers to the maximum comoving extent of the supercluster, and the mass indicates the total amount of baryonic and dark matter contained within the supercluster. As the luminosity and mass increase with time, the overall size decreases (Araya-Melo et al. 2009; Einasto et al. 2019, 2021a). The evolution of galaxies inside a supercluster is affected by its host supercluster's environment (Lietzen et al. 2012; Seth & Raychaudhury 2020; Alfaro et al. 2022). Also, the evolution of clusters and groups could be governed by the environment of the superclusters in which they reside. Extremely large superclusters may have a linear growth on average, but on a megaparsec scale, galaxies and clusters have a nonlinear growth within them. Overall, massive and large superclusters are excellent targets to study the diversity of environments they offer to their resident galaxies. Multiwavelength observations of such objects will aid our understanding of their growth and evolution. Ongoing and upcoming deep weak-lensing surveys will immensely help in estimating the masses of these huge overdensities.

In the Λ Cold Dark Matter (ΛCDM) model of the Universe, the overall growth of structures slows down below redshift $z \approx 0.5$ due to the influence of dark energy (Frieman et al. 2008; Einasto et al. 2021b). However, the highly overdense structures are still able to grow. In a spherical collapse model, structures that are at the turnaround stage at the present epoch, with a density contrast of $\sim$13.1, form bound systems. Structures with a present-day density contrast of $\sim$8.73 will reach the turnaround stage in the future (Einasto et al. 2020). Einasto et al. (2021c), using the spherical collapse model, suggested that structures with a present-day density contrast of $\approx$30 (rich clusters and their regions of influence in supercluster cores) have passed turnaround and started to collapse at redshifts $z \approx 0.3$–0.4. Therefore, a supercluster may or may not collapse, depending on the average density contrast of the entire supercluster. For example, Einasto et al. (2022) show that the BOSS Great Wall fragments into different structures in physical space, and these fragmented structures will collapse individually in the future.

In order to enhance our understanding of superclusters and their properties, it is important to identify these structures over a broad range of redshifts and a wide area of the sky. Moreover, their dynamical behavior can be explored using simulations. This paper presents 662 superclusters identified within a redshift range of $0.05 \leqslant z \leqslant 0.42$, covering a sky area of $\sim$14,000 deg^2. The properties of these superclusters are presented and compared with simulations. The layout of the paper is as follows. In Section 2, we present the observational data and mocks created through simulation. In Section 3, we present our analysis methods. In Section 4, we define the properties of the superclusters. Section 5 presents the results of our analysis. The properties of the identified superclusters highlighting the most massive superclusters (e.g., the Corona Borealis (CB) supercluster: Einasto et al. 2021c; the Sloan Great Wall (SGW): Gott et al. 2005; and the Saraswati supercluster: Bagchi et al. 2017), a power-law relation between the density contrast and the size of the supercluster, and the effect of the supercluster environment on the cluster properties are presented in Section 5.1. A comparison of the properties of superclusters extracted from observations and simulations and the phase-space distribution of the mock superclusters is presented in Section 5.2. We conclude and discuss the future prospects in Section 6, and the Appendix highlights the five most massive superclusters.

Throughout this paper, we have adopted the following cosmological parameters: $H_0 = 72$ km s^{-1} Mpc^{-1}, $\Omega_m = 0.26$, and $\Omega_\Lambda = 0.74$. $R_{\Delta c}$ is defined as the radius of a spherical region within which the matter density is Δ times the critical density (ρ_c) of the Universe. $M_{\Delta c}$ is the mass within this spherical region of radius $R_{\Delta c}$. So M_{500c} denotes the mass within a spherical region of radius R_{500c} where the mass density is 500 times the critical density of the Universe.

2. Data

Here, we describe the observational data and simulation used in our analyses.

2.1. Observational Data

Bagchi et al. (2017) used the spectroscopic sample of galaxies in the Sloan Digital Sky Survey (SDSS; York et al. 2000) to identify the massive supercluster named Saraswati. We have been motivated by the large excess of clusters and groups (Wen et al. 2012) found in the Saraswati

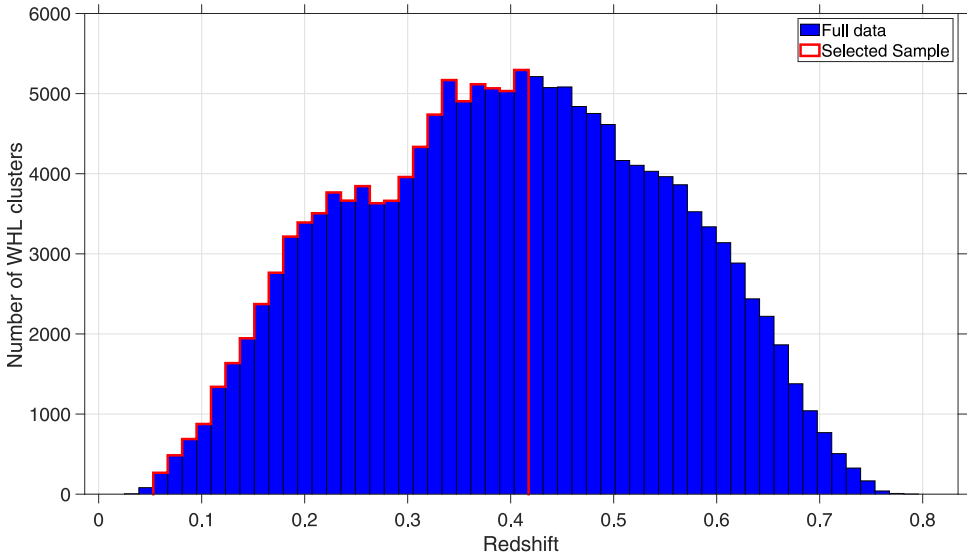

Figure 1. The blue histogram represents the redshift distribution of the entire sample of 158,103 WHL clusters, and the red line represents the selected sample of 85,686 clusters within the redshift range of $0.05 \leqslant z \leqslant 0.42$.

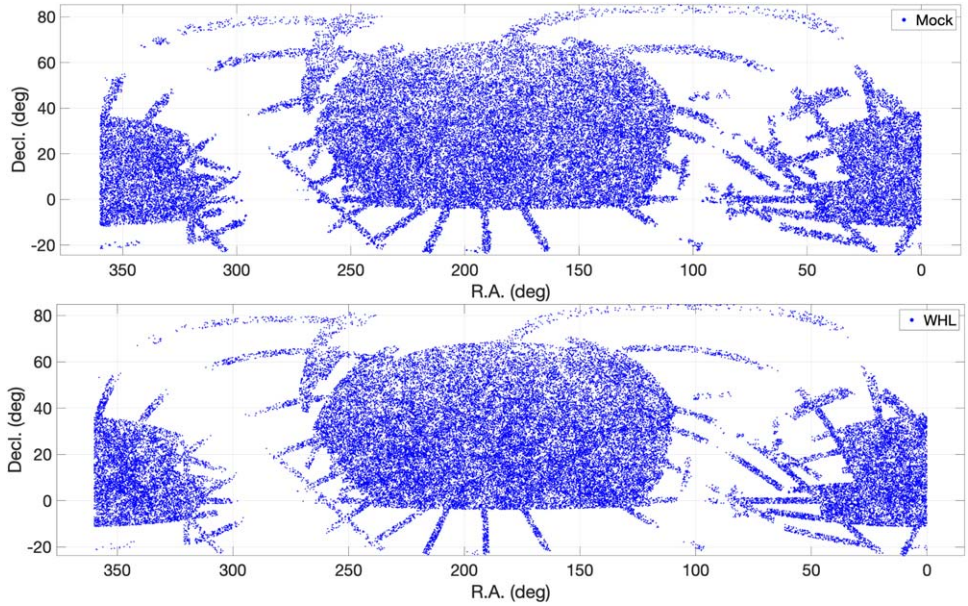

Figure 2. Sky distribution of the WHL clusters and HR4 halos within $0.05 \leqslant z \leqslant 0.366$. The WHL clusters and HR4 halos are the observed and mock samples, respectively.

supercluster region (Bagchi et al. 2017). As a result, we decided to search for other superclusters in SDSS using the same cluster catalog.

To achieve this, we use the group and cluster catalog of Wen & Han (2015; hereafter, WH15),[11] which is an updated version of Wen et al. (2012; hereafter, WHL12).[12] The WHL12 catalog consists of 132,684 groups and clusters identified from the photometric redshift data of galaxies within the redshift range $0.05 \leqslant z \leqslant 0.8$ from SDSS-III.[13] Galaxies with deblending problems and saturated objects were excluded. With the release of SDSS Data Release 12 (DR12; Alam et al. 2015), new spectroscopic redshifts of galaxies became available, leading to the addition of 25,419 rich clusters (primarily at high redshifts, $z > 0.4$) in the WH15 catalog.

In this paper, we utilize the spectroscopic redshifts available in DR12 for 89% of the groups and clusters listed in the WH15 catalog. For the remaining 11% of groups and clusters, we rely on photometric redshifts. Figure 1 shows the redshift distribution of WH15 groups and clusters. The small peak observed at $z \sim 0.22$ and the dip at $z \sim 0.28$ are attributed to the redshift distributions of the two major samples (the luminous red galaxy (LRG) and LOWZ galaxy samples) comprising SDSS. The LRG sample exhibits an increase beyond $z \sim 0.2$, while the LOWZ sample peaks at $z \sim 0.35$. The data set covers a sky area of $\sim$14,000 deg^2, as shown in Figure 2.

[11] https://cdsarc.cds.unistra.fr/viz-bin/cat/J/ApJ/807/178
[12] https://cdsarc.cds.unistra.fr/viz-bin/cat/J/ApJS/199/34
[13] https://www.sdss3.org

Table 1
Properties of 85,686 Groups and Clusters Extracted from the WHL Cluster Catalog within the Redshift Range $0.05 \leqslant z \leqslant 0.42$

ID	RA (deg)	Decl. (deg)	z	R_{200c} (Mpc)	M_{200c} ($10^{14}\,M_{\odot}$)	SCl
(1)	(2)	(3)	(4)	(5)	(6)	(7)
J000000.6+321233	0.00236	32.20925	0.1274	1.72	5.9478	0
J000002.3+051718	0.00957	5.28827	0.1694	0.94	1.9627	0
J000003.5+314708	0.01475	31.78564	0.0916	0.94	1.6766	0
J000004.7+022826	0.01945	2.47386	0.4179	0.95	0.4769	0
J000006.0+152548	0.02482	15.42990	0.1731	1.13	1.5391	0

Note. Columns (1)–(4) are taken from the WHL catalog and columns (5)–(7) have been computed in the current paper (see Sections 3 and 4). Column (1): cluster identifier. Column (2): R.A. of the brightest cluster galaxy (BCG). Column (3): decl. of the BCG. Column (4): redshift of the BCG. Column (5): R_{200c} of the cluster. Column (6): M_{200c} of the cluster. Column (7): supercluster number to which the cluster belongs. SCl = 0 means the cluster is not a part of any supercluster.

(This table is available in its entirety in machine-readable form.)

The completeness of the data, defined as the detection rate of the injected mock clusters using the cluster detection algorithm, depends on the virial mass M_{200c}. For clusters with mass $M_{200c} \gtrsim 0.6 \times 10^{14}\,M_{\odot}$, the completeness is ∼80% (WHL12). For clusters with $M_{200c} > 10^{14}\,M_{\odot}$, it exceeds 95%, and it reaches 100% for clusters with $M_{200c} > 2 \times 10^{14}\,M_{\odot}$ within the redshift range $0.05 \leqslant z \leqslant 0.42$. Consequently, we focus on the data within this redshift range, selecting 85,686 groups and clusters to extract superclusters (Figure 1). The false detection rate of these clusters is ≲6% (WHL12). For detailed group and cluster catalog construction information, refer to WHL12 and WH15. Throughout the rest of the paper, we will refer to the group and cluster catalog of WH15 (the updated WHL12 catalog) as the WHL cluster catalog. Table 1 shows the sample of selected 85,686 groups and clusters within the redshift range $0.05 \leqslant z \leqslant 0.42$.

The halo masses in WH15 are derived from the optical richness, which was cross-calibrated using clusters having masses from X-ray and Sunyaev–Zeldovich measurements. The optical richness is not expected to have a one-to-one correlation with the halo mass, but will instead be a useful proxy, rather than being entirely perfect and a proxy that will involve an intrinsic scatter. Therefore, a selection of clusters that are volume-limited by mass cannot be obtained in practice. In addition, the various flux limits of spectroscopic and photometric surveys will imply that the members of the clusters at higher redshift will be limited to brighter galaxies, which, on average, will be hosted by more massive clusters. In principle, such selection effects can be thoroughly included in the mocks, but such an implementation will require a cluster catalog that calibrates both the mean and the scatter of the richness–mass relation, accounting for the flux limit effects mentioned above. In the absence of such calibration, including the intrinsic scatter is beyond the scope of this paper, but is something that we plan to address in the future. In the current work, we treat incompleteness to be independent of mass and compensate for the incompleteness of low-mass clusters at higher redshift by increasing the linking length of the existing clusters. This allows the clusters to be linked at larger distances in inverse proportion to the cube root of their density (see Section 3) and ensures that the identification of superclusters is not affected by the incompleteness of the chosen sample. Additionally, we preferred to use all the data available in the WHL catalog, as applying a higher mass cut means that we have to discard some observational data. Instead, we use all the available observational data and model the incompletenesses in the data. This is the approach we have adopted here while constructing the mock catalog.

2.2. Simulation and Mock Clusters

We use the Horizon Run 4 (HR4) cosmological N-body simulation (Kim et al. 2015) to create a mock WHL cluster catalog. It has 6300^3 dark matter particles in a cubic box of size 3150 h^{-1} Mpc. The particle mass is $m_p \simeq 9 \times 10^9\,M_{\odot}$, and the minimum mass of halos with 30 member particles is $M_S \simeq 2.7 \times 10^{11}\,M_{\odot}$. The HR4 simulation adopted the Wilkinson Microwave Anisotropy Probe 5 yr (Dunkley et al. 2009) ΛCDM cosmology: $\Omega_{m,0} = 0.26$, $\Omega_{\Lambda,0} = 0.74$, and $H_0 = 100\,h$ km s^{-1} Mpc^{-1}, where $h = 0.72$.

In order to create a mock catalog, we require information on the position, mass, and peculiar velocity of halos. However, if we consider the snapshot of the simulation at redshift $z = 0$, it does not correspond to the observations that capture the states of objects at different cosmological times (redshifts). Essentially, a halo (or a cluster in observations) becomes visible to the observer when it enters the observer's past light cone (or the center of the simulation box). Therefore, we need to consider the state of a halo (its comoving position, mass, and peculiar velocity) at the time (redshift) when it enters the observer's past light cone. The HR4 simulation output products provide the necessary past light cone information on halos. We use the past light cone space dark matter halos in the redshift range $0 < z \leqslant 0.4$. We displace the halos according to their peculiar velocities to get the positions of halos in the redshift space (the same as the observations).

The mock WHL cluster catalog is made by selecting the halos according to the selection functions of the WHL cluster data. We matched the sky distribution, redshift distribution, and mass distribution of the WHL clusters for the extraction of halos from the HR4 simulation (see Figures 2 and 3). To make a sky mask for the WHL clusters' sky distribution, we use the Hierarchical Equal Area isoLatitude Pixelization (HealPix) scheme by Górski et al. (2005). HEALPix divides the sky plane into equal-area and shape-preserving pixels. We use $N_{\rm side} = 64$ and create the sky mask of the WHL catalog. A pixel is given an angular weight of 1 if it has at least one cluster in it and 0 if it does not contain any cluster. We then apply this mask to the HR4 halos and extract all the halos on the sky pixels with a weight equal to 1. Next, we divide the redshift distribution into equal comoving distance bins. In each bin, halos are extracted

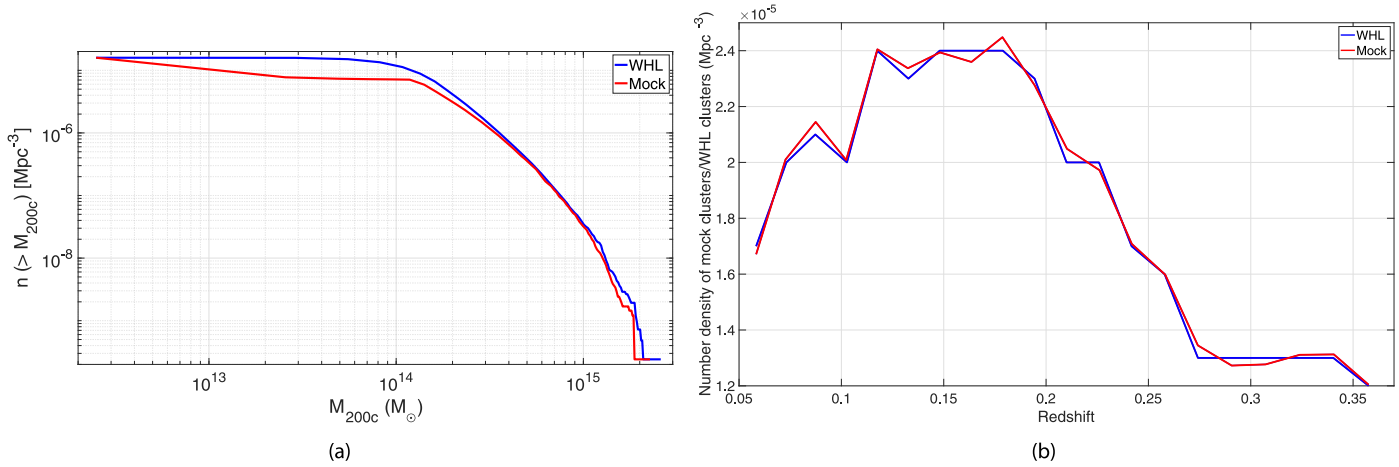

Figure 3. (a) Mass functions of WHL clusters and mock clusters (HR4 halos) within $0.05 \leqslant z \leqslant 0.366$. n is the number density of the clusters/halos. (b) Number density as a function of the redshift of the WHL and mock clusters (HR4 halos) within $0.05 \leqslant z \leqslant 0.366$.

to match the mass distribution and the number of WHL clusters in the corresponding bin.

Last, we find a small deficiency of large-mass clusters in the HR4 simulation compared to the WHL clusters. A similar deficiency with high-luminosity galaxies (the high-mass end of galactic halos) is also seen in other studies (see Trayford et al. 2015; Tuominen et al. 2021). To address this issue, when we encounter a deficiency of large-mass clusters within a specific distance bin, we randomly select halos from the lower-mass bin. However, we only choose halos that have not already been selected for the previous mass bin within that specific distance bin. This ensures that the number of mock clusters in each distance bin approaches the number of WHL clusters present in that particular distance bin. As a result, there is a small difference in the mass distribution between the WHL and mock clusters.

Additionally, to avoid the artificial change in the number density of halos at $z \sim 0.4$ due to the peculiar velocities of the galaxies in the halos, we have limited the halos to $0.05 \leqslant z \leqslant 0.366$. The redshift limit of 0.366 is chosen to avoid any contamination due to redshift space distortion by assuming a maximum peculiar velocity of a galaxy in a massive cluster as 5000 km s^{-1}. To err on the side of caution and ensure no contamination from the Fingers-of-God effect, a conservative value of 10,000 km s^{-1} (corresponding to $\Delta z \sim 0.034$) has been chosen. Figure 3 shows the mass and redshift distributions of the mock and WHL clusters.

3. Methods: Modified Friends of Friends

To identify the superclusters and create a supercluster catalog, a modified FoF (mFoF) algorithm is used. The FoF algorithm (Huchra & Geller 1982; Martínez & Saar 2002) finds overdensities in the distribution of galaxies or clusters. In this algorithm, a linking length l (threshold distance) is chosen. Two clusters are considered linked (part of the same supercluster) if the distance between them is less than or equal to l. This gives a system of clusters (a supercluster) with all the member clusters having distances to their natural neighbors $\leqslant l$. We modify the FoF algorithm to account for the selection biases in the survey. The mFoF algorithm makes use of Delaunay triangulation for distance calculations and weighted linking length to find the member clusters. The procedure is described below in detail.

3.1. Distances Using Delaunay Triangulation

A simple way is to calculate $O(N^2)$ distances for a distribution of N clusters and then find l for which the number of superclusters is maximum (see Section 3.4). This method is computationally very expensive for large values of N. To increase the computational efficiency, Delaunay triangulation (Delaunay 1934) is used to link a cluster to its nearest neighbors, and only the distances between the natural neighbors are considered. This reduces the calculation of $O(N^2)$ distances to $O(N\log N)$.

3.2. Radial Selection Weights

As the number density of WHL clusters varies with redshift, the distribution of WHL clusters is not uniform in the radial direction. The number density $\phi(z)$ of WHL clusters is shown in Figure 4. The radial selection weight $w_{r,i}$ of the ith cluster at redshift z is defined as

$$w_{r,i} = \frac{\bar{\phi}}{\phi(z)}, \tag{1}$$

where, $\bar{\phi}$ is the mean number density of the survey.

3.3. Weighted Linking Length

The number density of clusters varies with redshift (Figure 4), necessitating the adjustment of the linking length according to this variation. Consequently, the linking lengths will be different for different pairs of clusters. The radial selection weights are computed through three-dimensional density estimations. Therefore, the cube root of the weights is to be taken to apply these weights on the one-dimensional linking length:

$$w_{f,i} = [w_{r,i}]^{\frac{1}{3}}. \tag{2}$$

The final weights $w_{f,i}$ of all the clusters as a function of redshift are shown in Figure 4.

Now, if l_o is the selected linking length (as defined in Section 3.4), then the weighted linking length l_{ij} between the ith and jth

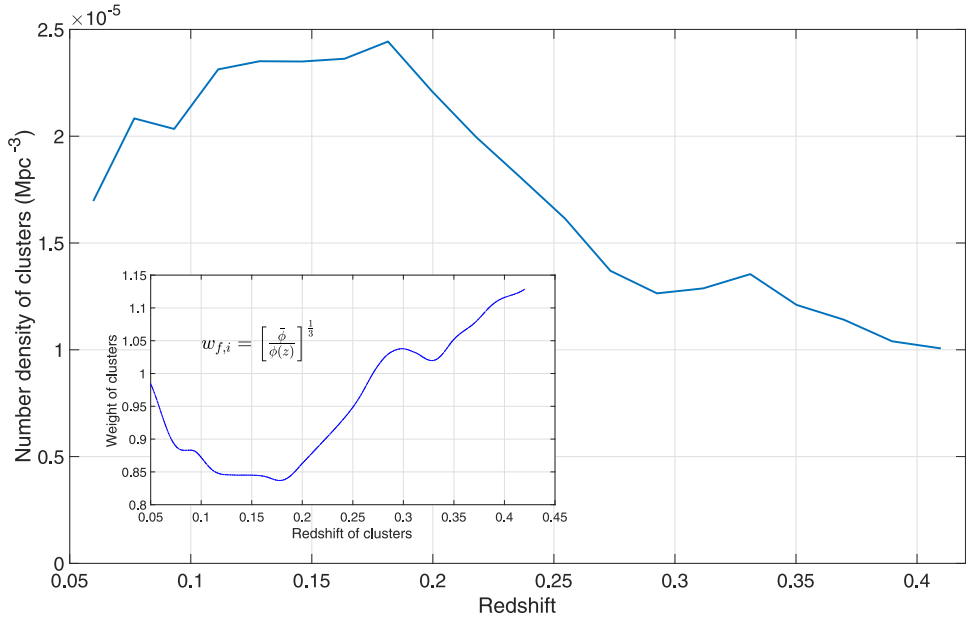

Figure 4. Number density $\phi(z)$ of WHL clusters as a function of redshift within $0.05 \leqslant z \leqslant 0.42$. Inset: corresponding weights $w_{f,i}$ of the clusters as a function of redshift.

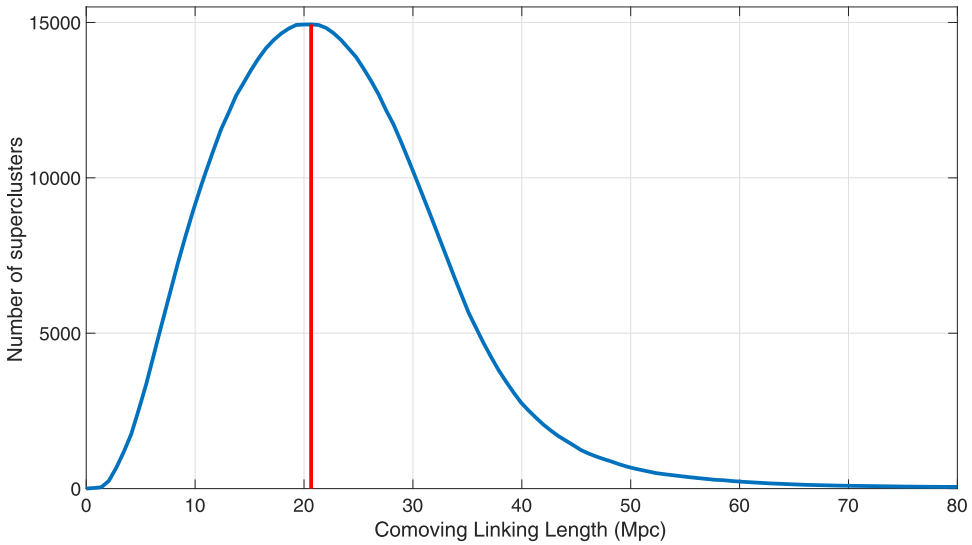

Figure 5. Number of candidate superclusters as a function of unweighted comoving linking length l_o (in blue). The red line shows the position $l_o = 20.65$ Mpc where the number of candidate superclusters is maximum.

clusters will be

$$l_{ij} = \frac{w_{f,i} + w_{f,j}}{2}\, l_o. \tag{3}$$

3.4. Selecting the Linking Length

The l_o is chosen to obtain the maximum number of superclusters for a given minimum number $N_{\rm min}$ of clusters in a supercluster (Chow-Martínez et al. 2014; Bagchi et al. 2017). In the literature, different FoF algorithms choose different $N_{\rm min}$ for clustering analysis, according to the data and the aim of the study. There are no fixed criteria for choosing $N_{\rm min}$, and the choice changes the value of the linking length and, thus, the clustering properties. In our analysis, we notice that selecting higher $N_{\rm min}$ values and subsequently calculating the linking length leads to unstable results, with the linking lengths varying significantly. We are limited by the number density of WHL clusters, and choosing a higher $N_{\rm min}$ value increases the statistical noise. Moreover, a higher $N_{\rm min}$ gives a higher linking length value, which leads to the identification of some spurious superclusters exceeding 600 Mpc in size, comprised of up to 200 member clusters and displaying negative density contrast values (indicating underdense regions). This issue persists even when considering only the nonstriped, contiguous survey region (discussed below). We mitigate this issue by choosing a lower value of $N_{\rm min} = 2$, which anchors the linking length estimation toward lower values, thereby preventing it from reaching percolation thresholds. For our analysis, the chosen linking length (l_o) for the sample is 20.65 Mpc (as shown in Figure 5), representing the maximum number of superclusters detected with $N_{\rm min} = 2$.

The above method gives a range of masses of superclusters with at least two clusters in a supercluster, and hence these can

be regarded as only candidate superclusters. The candidate superclusters with at least 10 member clusters are defined as superclusters in our catalog. The majority (∼80%) of clusters in the WHL catalog have masses $M_{200c} \gtrsim 10^{14} M_{\odot}$. With a minimum of 10 member clusters, the lower mass limit of a supercluster corresponds to $\sim 10^{15} M_{\odot}$. Consequently, all the superclusters included in our catalog have masses $\gtrsim 10^{15} M_{\odot}$, which is consistent with the findings regarding supercluster masses presented in Araya-Melo et al. (2009).

To verify the robustness of our analysis results against the complex geometry of our sample's sky footprint, we conducted an additional check by examining only the contiguous regions of our sample footprint, excluding the striped regions. We then performed the mFoF algorithm to detect superclusters. We found no significant deviations in the properties of the detected superclusters when comparing them to the findings presented in Section 5.1 for the entire survey footprint (as illustrated in Figure 2). This suggests that the inclusion of the striped regions in our analysis is justified. Furthermore, the detected superclusters in the striped regions will be useful for individual studies. Only 10 of our catalog's 662 superclusters (Section 5.1) are found within the striped regions. We also note that the very massive Saraswati supercluster was found in the narrow Stripe 82 of SDSS (Bagchi et al. 2017).

4. Properties of the Superclusters

4.1. Mass Estimation

In order to calculate the total mass of a supercluster, we use the following method. First, we calculate the bound mass of the individual member clusters of a supercluster. Then, we add the bound masses of all the member clusters to get the total mass of the supercluster.

WH15 provides information about clusters' richness in their catalog, denoted as $R_{L*,500}$. This richness is the optical luminosity, L_{500}, measured in units of L^*, the evolved characteristic luminosity of galaxies in the r band, within R_{500c}. WH15 also gives the correlation between the mass M_{500c} (in units of 10^{14} $M_{\odot}$) and richness $R_{L*,500}$ of the clusters as

$$\log M_{500c} = (1.08 \pm 0.02) \log R_{L*,500} - (1.37 \pm 0.02). \quad (4)$$

The mass uncertainty estimated by $R_{L*,500}$ is $\sigma_{\log M_{500c}} = 0.14$. To estimate the mass M_{500c} of a cluster, we utilize $R_{L*,500}$ in conjunction with Equation (4).

The relation between R_{200c} and R_{500c} is $R_{500c} \approx 0.65 \times R_{200c}$ for a given Navarro–Frenk–White mass profile with a concentration parameter in the range 4–8 (Ettori & Balestra 2009). And assuming a spherically symmetric distribution ($M_{\Delta c} = \Delta\, \rho_c \frac{4\pi}{3} R_{\Delta c}^3$) of halo density, M_{200c} can be expressed as

$$M_{200c} = \frac{200}{500} \left(\frac{R_{200c}}{R_{500c}} \right)^3 M_{500c}. \quad (5)$$

Using Equations (4) and (5), we get M_{200c} for each cluster. To account for the mass beyond the virial radius of a cluster, the virial mass (M_{200c}) of each member cluster is further scaled up by a factor of 2.2 to get its bound halo mass $M_{\rm halo} \approx M_{5.6c}$. In earlier studies, it is found that the bound halo mass of a cluster is close to $M_{5.6c} \sim 2.2 \times M_{200c}$ (Busha et al. 2005; Rines & Diaferio 2006; Rines et al. 2013). The sum of the bound halo masses of all the member clusters gives the total mass of the supercluster. Figure 6 shows the mass distribution of the superclusters.

4.2. Size and Position

The comoving linear size of a supercluster is calculated by measuring the maximum distance between pairs of member clusters of a supercluster. The comoving position $\boldsymbol{X}$ of the supercluster is taken as the virial mass-weighted average of the positions of member clusters,

$$\boldsymbol{X} = \frac{\sum_i M_{200c,i}\, \boldsymbol{X}_i}{\sum_i M_{200c,i}}, \quad (6)$$

where $M_{200c,i}$ and $\boldsymbol{X}_i$ are the virial mass and comoving position of the ith member cluster. The distributions of the superclusters' size, mass, and redshift are shown in Figure 6.

4.3. Density Contrast

To estimate the average density contrast δ of a supercluster, we now need to estimate the volume occupied by a supercluster. Since these superclusters do not have any specific shape, we estimate the volume by fitting a convex hull to the member clusters. A convex hull of a set of points P in three-dimensional Euclidean space is the convex surface (envelope) of the minimum possible volume on P. The volume of a supercluster is much larger than the volume of a single cluster. Hence, treating clusters as points or spherical objects with fixed radii has negligible impact on the estimated supercluster volumes. We use the Qhull algorithm (Barber et al. 1996) to construct the convex hull and to calculate its volume. Once we have the mass and volume, we can calculate the density of the supercluster. The corresponding matter density contrast, therefore, will be given by

$$\delta = \frac{\rho_{\rm SC}}{\rho_m} - 1, \quad (7)$$

where ρ_{SC} is the mass density of the supercluster and ρ_m is the background matter density at the redshift (z) of the supercluster:

$$\rho_m = \frac{3 H_0^2 \Omega_m (1+z)^3}{8\pi G}. \quad (8)$$

Figure 6 shows the density contrast of the superclusters.

5. Results

5.1. Observation

5.1.1. WHL Superclusters

The mFoF algorithm with at least 10 member clusters gives a total of 662 superclusters in the redshift range of $0.05 \leqslant z \leqslant 0.42$. To the best of our knowledge, this is the largest supercluster catalog constructed from the data of clusters in this redshift range. Around 12% of clusters (9895 clusters) from the WHL catalog considered for our work reside in a supercluster environment, and around 28% (183 superclusters) of the superclusters have at least one Abell cluster (Abell et al. 1989) in them. The presence of Abell clusters in many superclusters (for example, the Shapley supercluster: Shapley 1930; Raychaudhury 1989; the SGW; the Saraswati supercluster; and the CB supercluster) demonstrates the

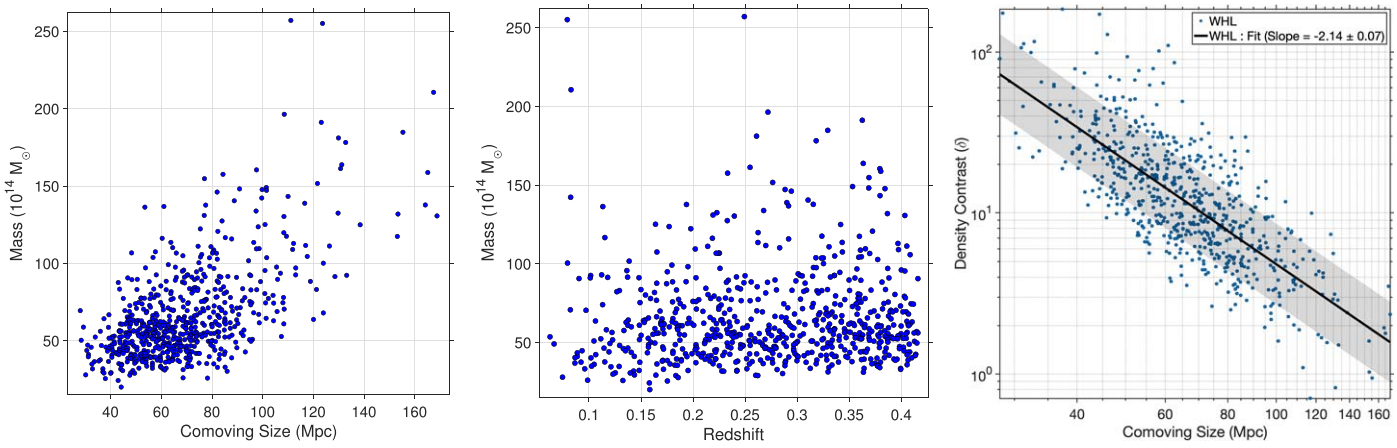

(a) (b) (c)

Figure 6. (a) Distribution of the superclusters' mass and size. (b) Distribution of the superclusters' mass and redshift. (c) Density contrast of the superclusters as a function of size. The blue dots represent the superclusters, the solid black line is a linear fit to the data points on the log–log plot, and the shaded black region denotes the associated errors in the fit. The slope of the fitted line is given at the top right corner of the plot.

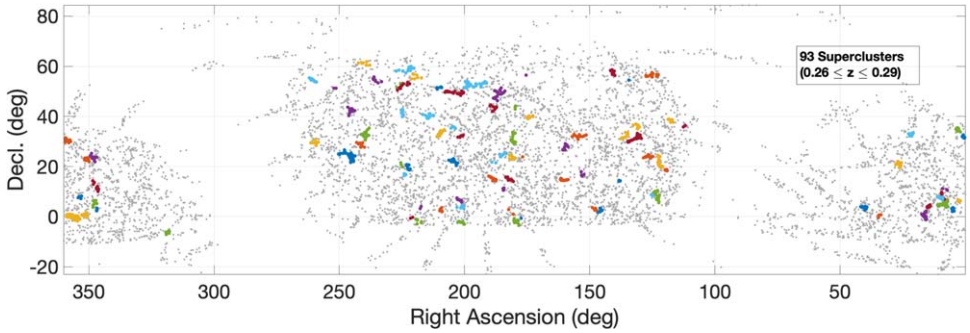

Figure 7. Sky plane distribution of the superclusters within $0.26 \leqslant z \leqslant 0.29$. The dots represent the WHL clusters within the redshift slice. The gray dots are not a part of any supercluster, and the other colored dots represent the member clusters of 93 superclusters within the redshift slice.

Table 2
Properties of the Sample of 662 Superclusters in Decreasing Order of Their Masses

SCl	R.A. (deg)	Decl. (deg)	RA_BCG (deg)	Decl_BCG (deg)	z	Size (Mpc)	Mass (10^{14} $M_\odot$)	$N_{\rm mem}$	$N_{\rm Abells}$
(1)	(2)	(3)	(4)	(5)	(6)	(7)	(8)	(9)	(10)
1	209.6316	3.3618	210.2586	2.8785	0.2493	111.10	257.106	54	2
2	235.1322	28.2855	239.5833	27.2334	0.0792	123.59	255.164	57	7
3	200.3919	0.2291	202.7959	−1.7273	0.0828	167.40	210.629	41	10
4	356.0263	−0.0101	355.9481	0.2567	0.2719	108.50	196.421	38	1
5	3.2246	8.3751	3.1893	8.3964	0.3625	123.10	191.222	44	0

Note. BCG stands for brightest cluster galaxy. Column (1): supercluster identification number in our catalog. Column (2): R.A. Column (3): decl. Column (4): R.A. of the most massive member cluster's BCG. Column (5): decl. of the most massive member cluster's BCG. Column (6): redshift. Column (7): linear comoving size. Column (8): total mass. Column (9): number of member clusters. Column (10): number of Abell clusters present.

(This table is available in its entirety in machine-readable form.)

robustness of our supercluster catalog. Figure 7 shows the distribution of the superclusters in the redshift slice $0.26 \leqslant z \leqslant 0.29$. All the WHL clusters within the redshift slice are represented by dots. Gray dots represent the clusters that are not part of any supercluster. The other colored dots represent member clusters of 93 superclusters within the redshift slice. The supercluster in yellow at $350^\circ \leqslant$ R. A. $\leqslant 359^\circ$ and decl. $\sim 0^\circ$ is the Saraswati supercluster.

The sky coordinates, redshifts, and properties of the superclusters, arranged in decreasing order of their masses, in our catalog are listed in Table 2. The distributions of the superclusters' mass, size, and density contrast are shown in Figure 6.

Apart from a few superclusters, which are rediscoveries of previously known superclusters, most of the superclusters reported here are newly discovered. For example, the Saraswati supercluster (SCl 4 and SCl 231) and the SGW (SCl 3 and SCl 22) are identified by our algorithm (see Section 5.1.2).

The median size and mass of the superclusters in our catalog are ∼65 Mpc and $\sim 6 \times 10^{15}\,M_\odot$, respectively. It is to be noted that the superclusters listed in our catalog might even be larger and more massive than currently indicated. We estimate the

masses of these superclusters by adding the bound masses of their member clusters. However, matter also exists between these clusters within a supercluster. Currently, we do not have an estimation of the mass attributed to this intercluster matter. Consequently, the actual mass of the superclusters may be higher than what is indicated by our calculations. In this context, Bagchi et al. (2017) found that if one assumes that the average density of diffuse matter (baryonic plus dark matter) dispersed between component (member) clusters is minimally at the cosmological matter density, then there is an increase in the total mass of the Saraswati supercluster at least by a factor of 2. Furthermore, it is worth considering that the superclusters situated at the edges of the SDSS survey footprint and those near the redshift limits of our sample might only be partially identified in terms of their true extent. Therefore, factors such as survey boundaries and limitations imposed by redshift constraints could potentially impact our ability to capture the entirety of these superclusters fully. A very deep and dedicated spectroscopic survey is needed to unravel their true extent and content. This sample will also be useful for comparing similar studies using numerical simulations. Also, since the catalog has a relatively wide range of redshift coverage, spanning ∼4 Gyr, the study of the evolution of the properties of galaxies in supercluster environments can be explored.

Our supercluster catalog differs in some ways from two other catalogs: the one by Chow-Martínez et al. (2014) and the other by Liivamägi et al. (2012). In the catalog by Chow-Martínez et al. (2014), the redshift coverage is less, up to $z \leqslant 0.15$. However, their sky coverage is significantly larger than ours, encompassing almost the entire sky, except for the Galactic disk region. To identify the superclusters, they implemented a tunable FoF algorithm based on the selection functions, applied to the Abell/Abell-Corwin-Olowin clusters (Abell 1958; Abell et al. 1989). The number of member clusters in their catalog varies from two to 42, and the sizes of the identified superclusters range from $<$ 1 Mpc to ∼185 Mpc. On the other hand, the supercluster catalog of Liivamägi et al. (2012) has a redshift coverage of $0.02 \leqslant z \leqslant 0.5$, but its sky coverage is less than 50% compared to our supercluster catalog. They took a different approach, identifying supercluster regions using the luminosity density field generated from the SDSS DR7 (Abazajian et al. 2009) spectroscopic galaxy data. Applying an adaptive density threshold on this field, they found supercluster sizes ranging from ∼22 to ∼260 Mpc. In contrast to these catalogs, our supercluster catalog provides additional information on mass estimates for the identified superclusters. Along with the wide sky coverage and comparatively large redshift range of our catalog, this additional information makes it a useful resource for further research and understanding of superclusters.

We also find a correlation between the density contrast and the size of the superclusters. It is close to a power law with an index $\alpha \sim -2$. The correlation (Figure 6) is

$$\log \delta = (-2.14 \pm 0.07) \log L + (4.95 \pm 0.13), \quad (9)$$

where δ is the density contrast and L is the size of the supercluster. In our catalog, we notice that this correlation arises from the dependency of mass (M) and volume (V) of the superclusters on its size ($M \propto L^{0.73}$ and $V \propto L^{2.64}$). It may arise due to the morphology distribution of the superclusters or due to the evolution of the superclusters/structures with time (Teerikorpi et al. 2015). We leave this aspect to explore in future work.

5.1.2. Notes on the Five Most Massive Superclusters

Here, we highlight the five most massive superclusters in our supercluster catalog. Figure A1 shows the sky distribution of these five superclusters. Figure A2 shows the optical images of the most massive member clusters of the top five superclusters in Table 2 from the DESI Legacy Imaging Surveys (DR9).[14] These are some of the richest clusters in the WHL cluster catalog. The WHL cluster catalog places the cluster ZwCl 2341.1+0000 (Figure A2—SCl 4) as the most massive cluster of the SCl 4 (Saraswati) supercluster. However, A2631 (also shown in Figure A2) is the most massive cluster of Saraswati (Bagchi et al. 2017; Monteiro-Oliveira et al. 2021). Zwcl 2341.1+0000 is a multiple-merger system (Bagchi et al. 2002; van Weeren et al. 2009; Boschin et al. 2013; Parekh et al. 2022), which is why the mass estimation of this cluster is slightly higher. Individual notes on the top five superclusters are given below:

SCl 1—new discovery. The most massive supercluster (SCl 1) is found at redshift ∼0.25 with mass $\sim 2.57 \times 10^{16} M_{\odot}$ and size ∼111 Mpc. This supercluster contains 54 member clusters, including A1835 and A1801. A1835 is the most massive member cluster of SCl 1 (see Figure A2). A1835 is a massive cool core cluster (Ueda et al. 2017) with a very high mass of $\sim 10^{15} M_{\odot}$ (Schmidt et al. 2001; LaRoque et al. 2006) and a radio minihalo (Kale et al. 2015). SCl 1 is a newly discovered supercluster and is the most massive at this redshift. We propose naming SCl 1 the *Einasto Supercluster* in honor of Prof. Jaan Einasto.[15]

CB Supercluster—rediscovery. In our catalog, the richest (maximum number of member clusters) supercluster is SCl 2, with 57 member clusters, including seven Abell clusters, at redshift $z \approx 0.08$, mass $M \approx 2.55 \times 10^{16} M_{\odot}$, and size ≈124 Mpc. It contains most of the CB supercluster (Einasto et al. 2021a). Figure 8 shows the three-dimensional distribution of the 57 clusters of SCl 2 in comoving coordinate space. Einasto et al. (2021a) showed that the CB supercluster consists of two parts, weakly connected by a chain of galaxies and poor groups. They found that these parts will separate during future evolution in physical space and form two separate structures. One of them, which contains Abell clusters A2065, A2061/A2067, and A2089, will be one of the most massive bound systems in the local Universe (Einasto et al. 2021a). Our algorithm combines the CB supercluster with the supercluster A2142 (see Einasto et al. 2015, 2018, 2020 for details and references). As a result, the total mass of this double supercluster system in our catalog is twice as high as the sum of masses of the CB and A2142 superclusters according to the estimates in Einasto et al. (2015, 2021c). Also, A2142 is the most massive cluster in the CB supercluster in our catalog. It is worth mentioning that the inner structure of the CB supercluster is complicated. It consists of multiple clusters connected by low-density filaments, resembling a group of spiders (called a multispider in a morphological classification of superclusters in Einasto et al. 2011b). Overall, the CB supercluster has a

[14] https://www.legacysurvey.org

[15] Prof. Jaan Einasto is one of the pioneers of the cosmic web. He was one of the first to start systematic studies of superclusters and still actively contributes to the field.

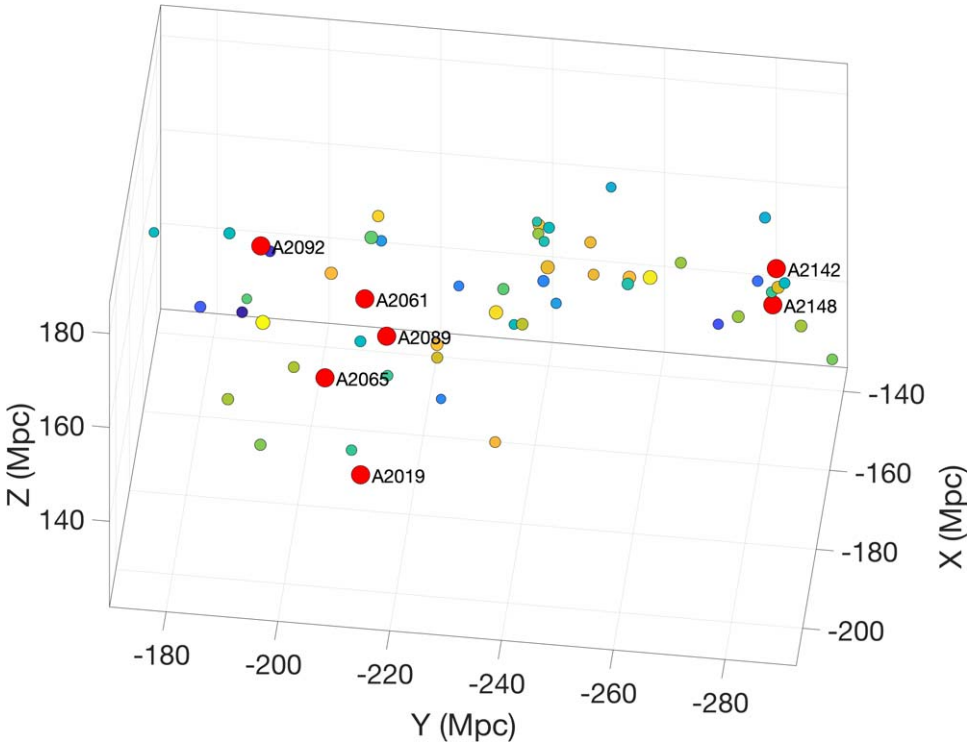

Figure 8. The three-dimensional distribution of clusters in the richest supercluster of our catalog (SCl 2), the CB supercluster. The colors represent the mass of the clusters, with blue representing the less massive clusters and yellow the most massive ones. The red spheres represent the Abell clusters; their Abell IDs are written next to them. There are a total of 57 clusters in SCl 2.

highly elongated shape, resembling a horseshoe (Einasto et al. 2011b).

SGW—rediscovery. The richest supercluster complex in the local Universe, the SGW is represented by two superclusters in our catalog, SCl 3 and SCl 22 (Figure A1). In Park et al. (2012), the spectroscopic galaxy data from SDSS is utilized to identify nearby structures. Due to the higher density of these data than our sparser cluster data, these superclusters have been identified as a single system (Park et al. 2012). The morphology of SCl 3, the richest SGW supercluster, resembles a multibranching filament with rich galaxy clusters connected by a small number of filaments. The second richest supercluster in SGW, SCl 22 in our catalog, is a multispider, in which clusters and groups are connected by a large number of filaments. During future evolution in physical space, both these superclusters will fall apart and form smaller superclusters (Einasto et al. 2016). SGW superclusters differ in galaxy content and morphology, suggesting that they have had different evolution (Einasto et al. 2010, 2011c).

Saraswati Supercluster—rediscovery. The Saraswati supercluster (Bagchi et al. 2017) is a massive supercluster surrounded by large voids at a redshift ∼0.28. In our catalog, it is identified with SCl 4 and SCl 231 (Figure A1). The total number of member clusters is 51 (38 clusters in SCl 4 and 13 in SCl 231). In Bagchi et al. (2017), a high-density spectroscopic galaxy sample was used to identify the Saraswati supercluster. This sample allowed them to observe a continuous structure encompassing SCl 4 and SCl 231. The combined mass of SCl 4 and SCl 231 is $\sim 2.6 \times 10^{16}\ M_{\odot}$, slightly higher than, but still within the same order of magnitude as, the value reported in Bagchi et al. (2017). The increased mass is attributed to the inclusion of more member clusters, made possible by the wider sky area coverage of the WHL cluster catalog compared to the spectroscopic galaxy sample used in Bagchi et al. (2017). The most massive cluster of Saraswati is A2631, and the second most massive cluster is ZwCl 2341+0000. Bagchi et al. (2017) showed that the central core region within a radius ∼20 Mpc of this supercluster, including A2631, is gravitationally bound. The total size of this supercluster is ∼200 Mpc, which is the largest supercluster at this redshift.

SCl 5—new discovery. SCl 5 is our catalog's fifth most massive supercluster, containing 44 clusters at a redshift ∼0.36. Its mass and size are $\sim 1.9 \times 10^{16}\ M_{\odot}$ and ∼123 Mpc, respectively. It does not contain any Abell cluster. It is also a newly discovered supercluster.

5.1.3. Effect of Supercluster Environment on the Clusters

The cosmic environment affects the growth and evolution of galaxies and clusters. To explore whether the supercluster environment plays any role in the evolution of clusters, we study the mass distribution of clusters in superclusters and in the field (clusters that are not members of any supercluster). The left panel of Figure 9 shows the normalized mass distributions of the member clusters of superclusters and the field clusters. It shows a slight mass bias of finding massive clusters in a supercluster environment rather than in the field. Similarly, there is a slight deficiency of less massive clusters within superclusters. In other words, the probability of randomly picking a massive cluster is slightly higher within a supercluster environment than in the field. And the probability of randomly picking a less massive cluster is slightly higher in the field than in a supercluster region. To see the difference between the two distributions, we perform a two-sample Kolmogorov–Smirnov test (Kolmogorov 1933; Smirnov 1948).

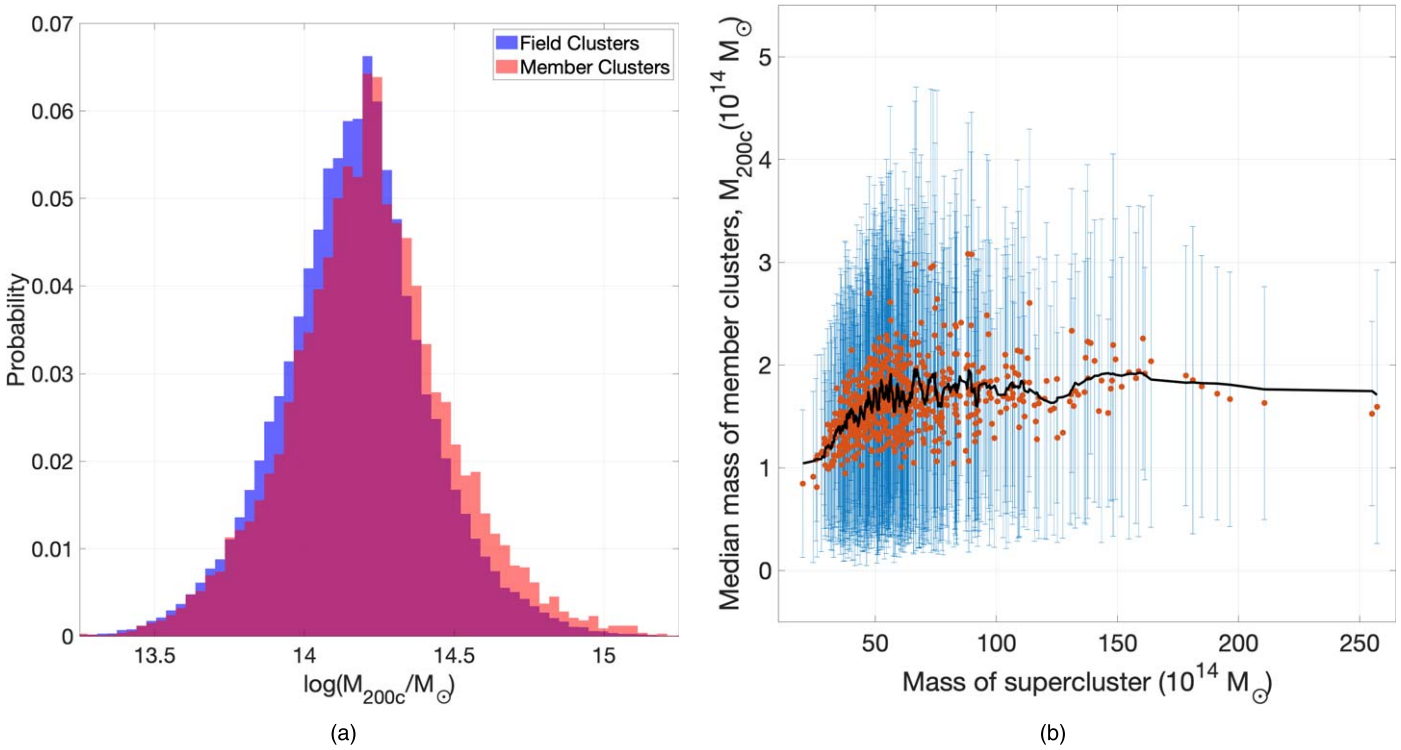

Figure 9. (a) Normalized histograms of the masses of clusters within superclusters (red histogram) and in the field (blue histogram). (b) Median masses (red dots) of the member clusters of superclusters as a function of their total mass. The blue error bars denote the quartile values of the member cluster masses above and below the median values, and the solid black line is the running mean of the red dots.

The null hypothesis that the two samples are drawn from the same population is rejected with a p-value of 3.7×10^{-52}. This shows that the supercluster environment affects the evolution of clusters.

We also explore the mass distribution of the member clusters within each supercluster. The right panel of Figure 9 shows the median values (red dots) of the mass of clusters in a supercluster as a function of the total mass of the supercluster. Here, despite a large scatter, we see a trend indicating that the low-mass superclusters (masses $\lesssim 5 \times 10^{15}\ M_{\odot}$) host low-mass member clusters. This may suggest that the growth of clusters is higher in high-mass superclusters. However, this growth in mass is not very high: the median value goes from $\sim 1 \times 10^{14}\ M_{\odot}$ to $\sim 1.8 \times 10^{14}\ M_{\odot}$.

5.2. Simulation

5.2.1. Comparison with Simulation

We compare our results with the mock superclusters extracted from the mock WHL clusters of the HR4 simulation (as described in Section 2.2). To compare the redshift coverage of the mock clusters, we restrict our observational data of the clusters to $0.05 \leqslant z \leqslant 0.366$. We then apply the same mFoF algorithm on the observed and mock clusters to identify superclusters. The results are summarized in Figures 10 and 11 and Table 3.

The distributions of the size, density contrast, and the number of member clusters match fairly well, but there is a slight difference in the distribution of masses of superclusters (Figure 10). The difference in the mass distributions is because of the deficiency of massive clusters in the mock WHL clusters made from the HR4 simulation (see Section 2.2).

The linking lengths for WHL and the mock clusters are 19.22 Mpc and 19.88 Mpc, respectively (Figure 11). This difference of 0.66 Mpc is acceptable, as it is much less than the mean cluster separation (∼40 Mpc) and less than the mean diameter of a cluster (∼2 Mpc).

We also see the correlation between the density contrast and the size of a supercluster in the mock superclusters (Figure 11). The value of the slope here is $\sim -2.04 \pm 0.10$.

5.2.2. Peculiar Velocities of Members in the Mock Superclusters

In Figure 12, we show the radial peculiar velocities as a function of their comoving distance from the centers of all the superclusters stacked in the reference frame of the center of mass of the supercluster. The radial peculiar velocity v_{pec} of a member cluster is

$$v_{\rm pec} = (\boldsymbol{v}_{\rm mem} - \boldsymbol{v}_{SC}) \cdot \hat{\boldsymbol{r}}, \tag{10}$$

where $\boldsymbol{v}_{\rm mem}$ is the peculiar velocity vector (as given in the HR4 simulation) of the member cluster, $\boldsymbol{v}_{SC}$ is the peculiar velocity vector of the center of mass of the supercluster, and $\hat{\boldsymbol{r}}$ is the comoving position unit vector of the member cluster in the frame of reference of the center of mass of the supercluster. Figure 12 shows the phase-space distribution of member clusters, where the y-axis shows the radial peculiar velocities (the peculiar velocity component of a member cluster in the reference frame of the center of mass and along the line from the center of mass to the member clusters) of the member clusters of all superclusters and the x-axis is the comoving distance of a member cluster from the center of mass of a supercluster. The black line represents a radial peculiar velocity of 0 km s^{-1} and the red line represents all the radial peculiar

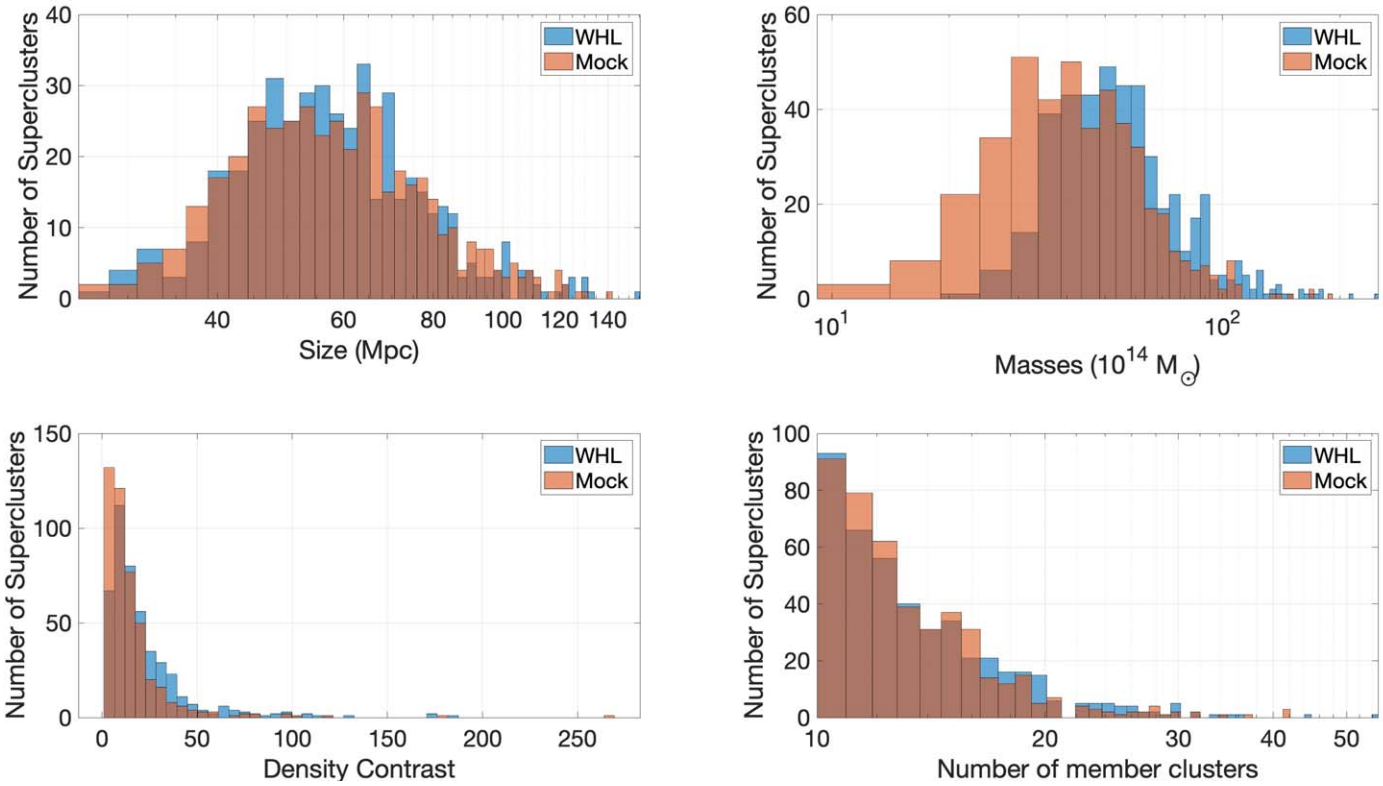

Figure 10. Distributions of the size, mass, density contrast, and the number of member clusters of the superclusters in WHL and HR4 within $0.05 \leqslant z \leqslant 0.366$.

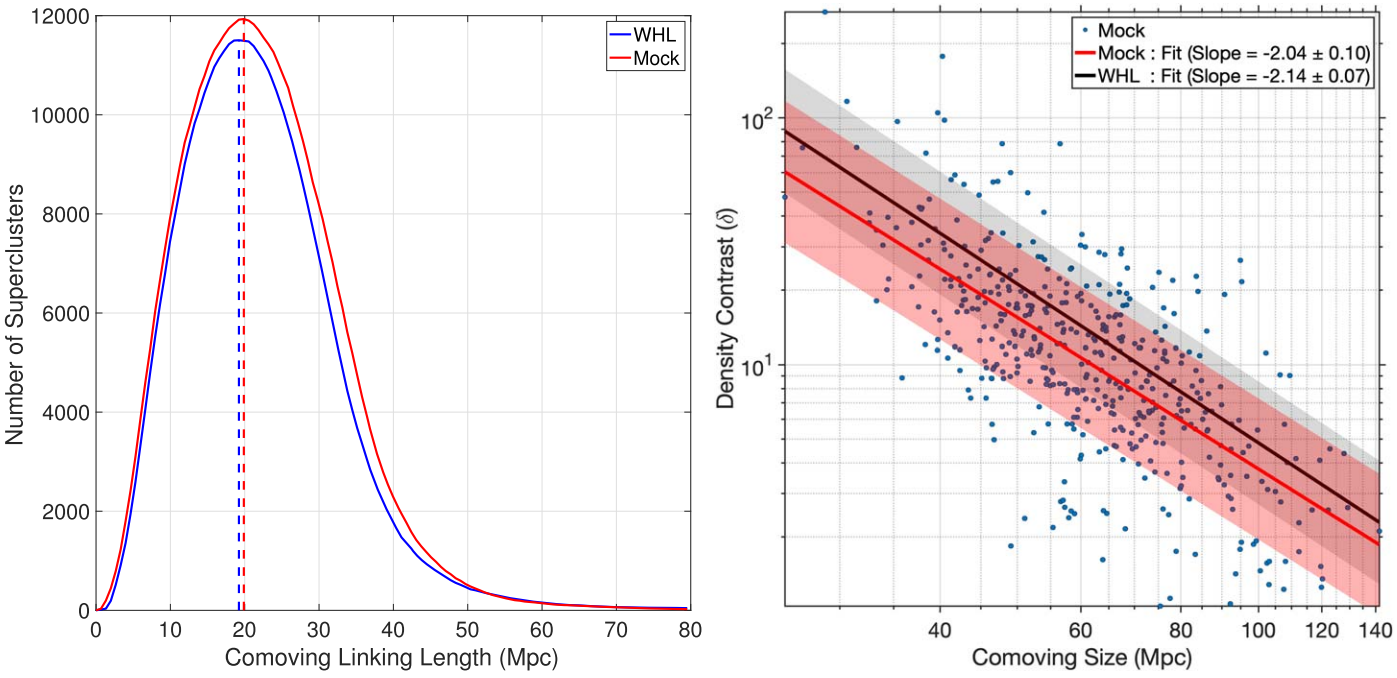

(a) (b)

Figure 11. (a) Number of candidate superclusters for different linking lengths l_0 for WHL and the mocks. The curves peak at 19.22 Mpc and 19.88 Mpc for WHL and the mocks, respectively, and are represented by dotted lines. (b) Density contrast of the mock superclusters as a function of size. The blue dots represent the mock superclusters, the red line is a linear fit to the data points on the log–log plot, and the shaded red region denotes the associated errors in the fit. The slope of the fitted line is given at the top right corner of the plot. The black line and the shaded black region denote the corresponding fit and the associated errors of WHL superclusters presented in Figure 6(c).

velocities equal and opposite to the Hubble flow as seen from the center of mass frame. The three regions divided by red and black lines tell us the kinematical state of the member clusters. *Hubble Decoupled*: member clusters that have decoupled from the Hubble flow and are moving toward the supercluster center; *Supercluster Influence*: member clusters that have not

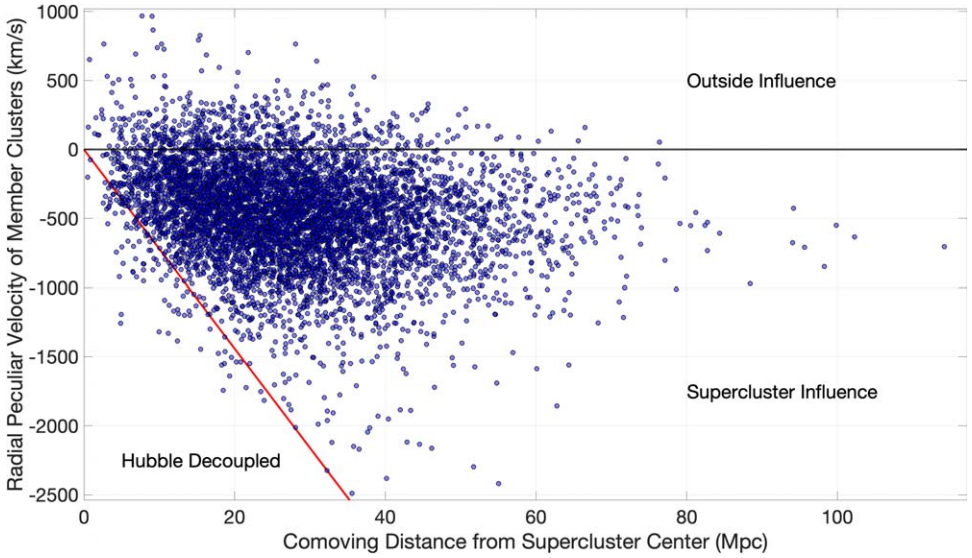

Figure 12. Radial peculiar velocities of the member clusters of all (stacked) superclusters as a function of their comoving distance from the supercluster center. The black line represents a peculiar velocity of 0 km s^{-1}, and the red line represents all the peculiar velocities equal and opposite to the Hubble flow as seen from the center. The three regions, divided by red and black lines, are *Hubble Decoupled*: members that have decoupled from the Hubble flow; *Supercluster Influence*: members that have not decoupled from the Hubble flow, but have slowed down in their Hubble expansion; and *Outside Influence*: member clusters that have their velocities greater than the Hubble flow and therefore have gravitational influence from regions outside of the supercluster.

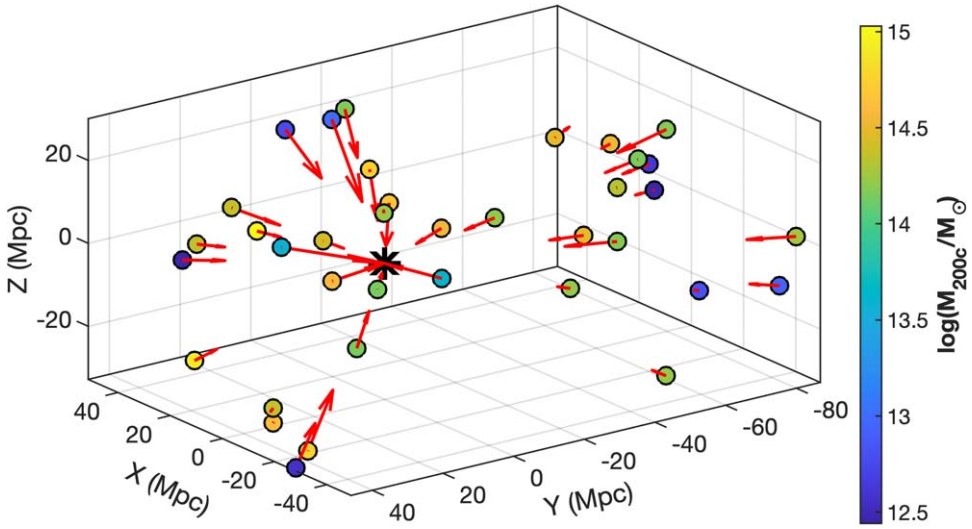

Figure 13. The most massive supercluster in the mock. The "∗" symbol indicates the center of mass of the supercluster. Member clusters are represented by circles and their colors indicate the masses M_{200c}. The red arrows show the supercluster-centric peculiar velocity components (radial peculiar velocities) of the member clusters, with arrow lengths proportional to the radial peculiar velocities. Here, an arrow with a length of 1 Mpc corresponds to 60 km s^{-1}.

Table 3
Summary of the Properties of the Observed and Mock Superclusters

	WHL ($0.05 \leqslant z \leqslant 0.42$)	WHL ($0.05 \leqslant z \leqslant 0.366$)	Mock ($0.05 \leqslant z \leqslant 0.366$)
Linking Length l_o (Mpc)	20.65	19.22	19.88
Number of Superclusters	662	456	451
Median Mass (10^{14} $M_\odot$)	57.80	55.97	46.43
Median Size (Mpc)	64.87	60.49	60.83
Median Density Contrast	11.64	15.40	10.88
Median No. of Members	13	13	12

decoupled from the Hubble flow, but have slowed down in their Hubble expansion; and *Outside Influence*: member clusters that have their velocities greater than the Hubble flow and therefore have gravitational influence from regions outside of the supercluster. On average, 89%, 9%, and 2% of the member clusters are in the regions of "Supercluster Influence," "Outside Influence," and "Hubble Decoupled," respectively. For example, Figure 13 shows the supercluster-centric spatial

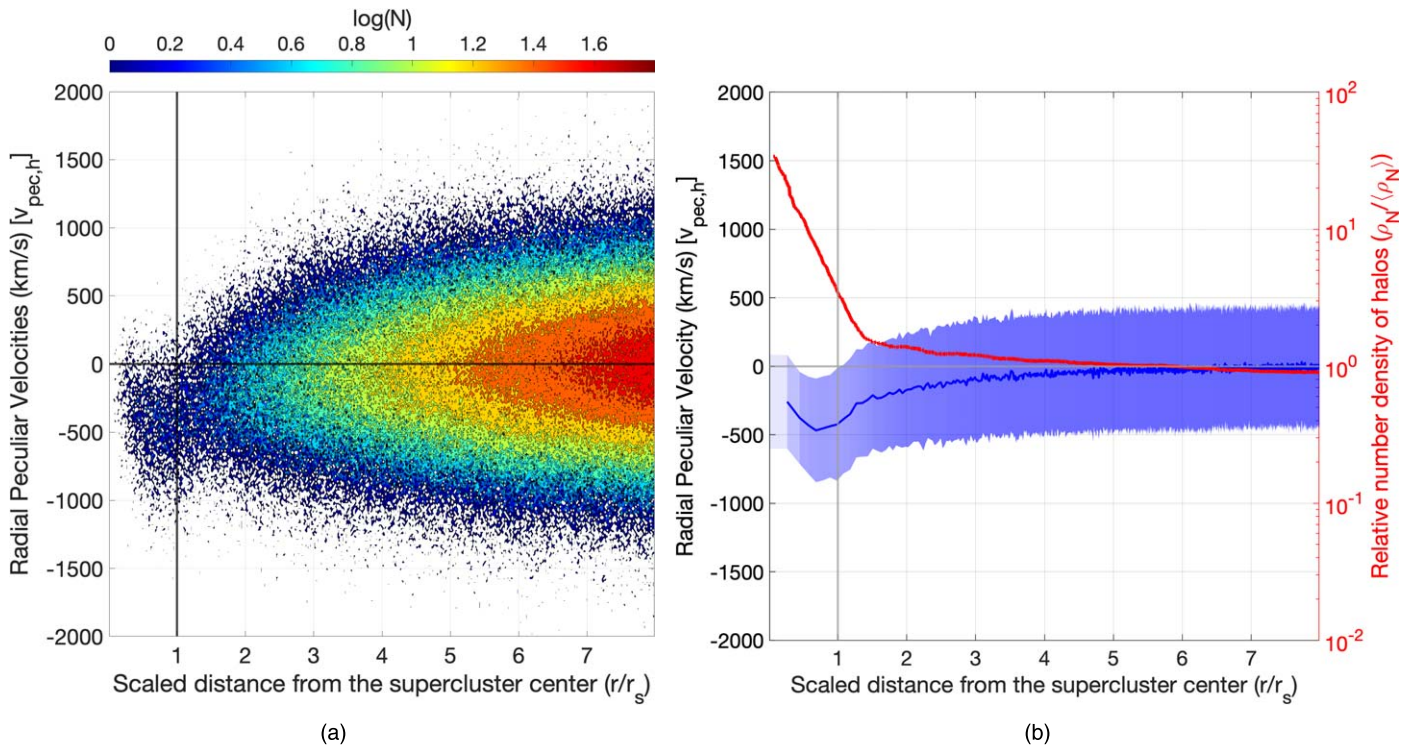

Figure 14. Stacked radial peculiar velocities and relative number density in and around superclusters. The x-axis denotes the distance from the supercluster center in units of r_s (half the size of a supercluster). (a) Two-dimensional histogram of the mock halos in and around superclusters. N denotes the number of halos in each grid. The region ($r/r_s \lesssim 1$ and $v_{\rm pec,h} \lesssim 0$) contains most of the member halos of a supercluster. (b) Mean (blue line) values of the radial peculiar velocity component as a function of scaled distance. The shaded blue region shows the standard deviation (1σ) of the radial peculiar velocity component. The red line shows the relative number density of halos as a function of scaled radius. This relative number density is calculated by dividing the average number density ρ_N (of all stacked superclusters) at a scaled radius by the total number density $\langle\rho_N\rangle$ of halos within a sphere of radius $\sim 8 \times r_s$.

distribution of the member clusters of the most massive supercluster in the mock. The arrows indicate the supercluster-centric peculiar velocity components (radial peculiar velocities), almost all pointing toward the supercluster center indicated by the "$*$" symbol.

5.2.3. Phase-space Distribution of Mock Halos in and around Superclusters

As shown in Figure 12, most supercluster member halos (91%) have a negative supercluster-centric peculiar velocity component. The member halos are influenced by the gravitational potential of their host supercluster. This influence should be negligible on the halos well outside the supercluster region. The phase-space distribution of halos within the supercluster region should be distinguishable from those outside the supercluster region. If we take the supercluster-centric peculiar velocity components of all halos from the supercluster center up to some distance outside the supercluster, we should see the overall negative components going to zero values at higher distances outside the supercluster. To explore this effect, we present the stacked supercluster-centric phase-space distribution in and around the supercluster region in Figure 14. The x-axis shows the scaled distance from the supercluster center. If S is the size of a supercluster, then we define a quantity, $r_s = S/2$, of a supercluster. The supercluster-centric comoving distances r of the halos are then scaled to r_s. This gives a unit-scaled distance as the rough extent of a supercluster. The left panel shows the two-dimensional histogram of the halos in and around the superclusters (stacked) up to a scaled distance, $r/r_s = 8$. In this panel, we can see that there is a detached distribution ($r/r_s \lesssim 1$ and $v_{\rm pec,h} \lesssim 0$) from the main distribution ($r/r_s \gtrsim 1$), where $v_{\rm pec,h}$ is the supercluster-centric peculiar velocity component of the halos. This detached distribution is the supercluster region where most halos have negative radial peculiar velocity components. Beyond the supercluster region ($r/r_s \gtrsim 1$), when it starts to encounter surrounding voids and other cosmic web components/structures, this distribution of the negative component of the peculiar velocity gradually and slowly moves toward zero.

The right panel of Figure 14 shows the mean values (blue line) of the radial peculiar velocities of halos at a certain scaled distance from the supercluster center. The shaded blue region shows the standard deviation (1σ) of the supercluster-centric peculiar velocity distribution above and below the mean values. It shows that at a distance approximately four to five times r_s, the value goes to the global average of zero, which is expected on larger scales. The red line shows the relative number density of halos as a function of the scaled distance. It is calculated by dividing the average number density ρ_N (of all stacked superclusters) at a scaled radius by the total number density $\langle\rho_N\rangle$ of halos within a sphere of radius $\sim 8 \times r_s$. Both the velocity and density profiles show a characteristic scale at a distance of $\sim 1.5 \times r_s$.

It should be noted that the superclusters in our catalog are not spherically symmetric, and the supercluster center, which is the barycenter of the member clusters, may not coincide with the geometric center of the supercluster. Because of this asymmetry, the characteristic scale is not $r/r_s = 1$ and comes out to be $r/r_s \sim 1.5$. After this characteristic scale, both profiles gradually approach their global values.

Figures 12 and 14 support the robustness of the superclusters identified in our catalog. The density contrast of all the superclusters in our catalog has values greater than zero. The relative density shows a knee around 1.5 times the scaled distance, also where the shape of the radial peculiar velocity profile changes. This suggests that these superclusters are well within the basin of attraction. The overall densities of the superclusters are not sufficiently high enough to classify them as gravitationally bound structures within the framework of a spherical collapse model. Instead, they are more likely to fragment into smaller structures, similar to the observed cases of the Saraswati supercluster (Bagchi et al. 2017) and the BGW supercluster (Einasto et al. 2022). We therefore conclude that our superclusters fall in the supercluster definition (2)—the unbound overdense regions in the Universe (see Section 1).

6. Discussion and Conclusion

Superclusters, being the largest structures in the Universe, need more focused multiwavelength studies than their current status of study. Whether they grow with a bottom-up process, a top-down process, or both needs to be addressed observationally as well as theoretically. Identifying superclusters and creating a statistically significant sample will increase our understanding of their properties and their environmental effects on the galaxies, groups, and clusters in them.

As the galaxy redshift surveys have become deeper and larger over time, not only more superclusters, but also bigger superclusters, have been discovered. Hence, it will not be surprising if even bigger superclusters are discovered in the upcoming redshift surveys like DESI (DESI Collaboration et al. 2016), 4MOST (de Jong et al. 2019; Richard et al. 2019), Euclid (Laureijs et al. 2011), etc. And this may pose a challenge to the ΛCDM model of the Universe (Park et al. 2012).

In this work, we have identified 662 superclusters in the redshift range $0.05 \leqslant z \leqslant 0.42$ using the spatial distribution of WHL clusters. We have applied an mFoF algorithm to overcome the survey/catalog selection effects. These superclusters have typical masses $>10^{15}$ $M_{\odot}$ and sizes >10 Mpc. *Einasto Supercluster*, a new discovery at $z \sim 0.25$, is found to be the most massive supercluster in our catalog.

In our process of identifying superclusters, we have rediscovered many previously known superclusters, as well as discovered many new ones. We found a power-law relation between a supercluster's density contrast and size with an index ~ -2. Whether this suggests a relation with the morphology of the supercluster or some other relation is a matter of further study. The topological analysis of the shape of superclusters may explain this phenomenon more clearly. Recently, Bag et al. (2023) found that large superclusters with volumes $\gtrsim 10^4$ Mpc^3 tend to be more filamentary, and Heinämäki et al. (2022) found that the low-luminosity, small, poor, and low-mass end of superclusters has pancake-type shapes, while only a handful exhibit exceptionally spherical shapes. The supercluster environment weakly affects the evolution of clusters. It is slightly more likely to find a massive cluster in a supercluster environment than in a nonsupercluster environment.

The simulation gives slightly fewer high-mass clusters than those found in the observations. This gives a difference in the mass distribution of halos/clusters in the simulation and observational data and affects our comparison of the properties of superclusters found in the simulations and observations. Nevertheless, we found almost comparable properties in the simulated and SDSS data. The peculiar velocity field of the mock superclusters in the simulation shows that the most part of a supercluster points toward the center of mass of the supercluster. That is, the most part of a supercluster is influenced by its mass and overdensity. This leads to a slowing down of the expansion of the supercluster with respect to the Hubble flow. The phase-space distribution of halos in and around the superclusters shows a characteristic length scale when a change in radial peculiar velocity and density profiles is seen. This length scale lies approximately 1.5 times the scaled distance from the supercluster center and arises due to the nonspherical shapes of the superclusters.

Superclusters host some of the most massive galaxy clusters formed through mergers. Under the right conditions, upon a merger, the resulting propagating shock manifests as megaparsec-scale radio relics (e.g., Bagchi et al. 2002, 2006; van Weeren et al. 2009) and radio halos (for a review, see van Weeren et al. 2019). Recently, using the eROSITA Final Equatorial Depth Survey, Ghirardini et al. (2021) reported a new supercluster at a redshift of $z \sim 0.36$ with eight associated galaxy cluster members and spanning ~ 27 Mpc. They have also carried out detailed X-ray, optical, and radio studies of the supercluster, where they found two new radio relics and a radio halo. The Shapley supercluster has been the subject of numerous multiwavelength studies in the past few decades. Its central part has recently been studied at radio wavelengths using sensitive observations from uGMRT, MeerKAT, and ASKAP (Venturi et al. 2022). In addition to finding radio halos and very low surface brightness radio emissions connecting groups and clusters (~ 1 Mpc), such deep multifrequency observations also enable estimation of the equipartition magnetic field (~ 0.76 μG) permeating across a large region. Hence, the study by Venturi et al. (2022) provides compelling evidence of nonthermal signatures detected from minor mergers (e.g., megaparsec-scale radio emission from bridges connecting clusters and groups).

Simulations show that supercluster embryos form at very early cosmological epochs. Even in observations, superclusters have been detected at higher redshifts, extending as far back as $z \sim 2.45$ (Kim et al. 2016; Lietzen et al. 2016; Cucciati et al. 2018; Shimakawa et al. 2023). The location of superclusters does not change much during evolution, and the essential evolutionary changes occur within the supercluster cocoons (basins of attraction or the regions of dynamical influence; Einasto et al. 2019, 2021a). On the question of the formation of the superclusters, Einasto et al. (2011a) and Suhhonenko et al. (2011), using wavelet analysis of the cosmic web, show that rich clusters and superclusters form where density waves of medium ($\simeq 32$ h^{-1}Mpc) and large scales ($\geqslant 64$ h^{-1}Mpc) combine in similar phases to generate high-density regions. They show that the synchronization (or coupling) of differently scaled density waves plays an important role in structure formation. Their results show that the largest structures to form have sizes of approximately 100 h^{-1} Mpc, which agrees with the size of the largest superclusters in our study. Density waves with larger scales only modify the properties of structures.

Underdense regions (voids) that surround superclusters form where different phases of the density waves are combined. Matter within the voids flows toward the inner regions of superclusters due to gravitational instability. Observationally,

this has been shown by analyzing local velocity fields (Tully et al. 2014; Hoffman et al. 2017). The voids may be expanding more rapidly than the global expansion rate and thus helping in the growth of the supercluster (Sheth & van de Weygaert 2004; van de Weygaert 2016; Bagchi et al. 2017; Hoffman et al. 2017). The expansion of large voids can facilitate shaping surroundings and help in the formation of long coherent structures (superclusters) along its boundary or periphery.

Superclusters are important to study the formation of structures on large scales. For further advances in this subject, a detailed spectroscopic survey of a massive supercluster is needed (e.g., the Saraswati supercluster), which can inform us more about the dynamical state of the supercluster. Such surveys will provide the crucial information needed to answer open questions in supercluster physics, provide a wealth of data for individual galaxies, and pave the path for more synergistic studies. Future deep, wide-sky galaxy surveys will provide the opportunity to compare the abundance and properties of superclusters at higher redshifts with the ones in simulations. Therefore, it is vital to identify and characterize superclusters. It is important to compare the properties of galaxies in large, high-density regions like superclusters and in underdense regions like voids to understand the factors affecting their growth and evolution. The current era of deep multiwavelength large sky surveys provides us with the perfect opportunity.

Acknowledgments

We thank the referee for the valuable and constructive comments, which have enhanced the paper's clarity and readability. S.S. acknowledges the support of the European Regional Development Fund, the Mobilitas Pluss postdoctoral research grant MOBJD660, and the ETAg grant PRG1006. E.T. and M.E. acknowledge the support from ETAg grant PRG1006 and EU through the ERDF CoE TK133. J.B. acknowledges the help and full support from Christ (Deemed to be) University in facilitating the research. We kindly thank Changbom Park, Sung-Wook Kim, and Juhan Kim for providing the HR4 simulation products on request.

Appendix
Five Most Massive Superclusters

Figure A1 shows the sky plane distribution of the five most massive superclusters. The member clusters are shown with their sizes proportional to their R_{200c}, and the color scale indicates their masses (M_{200c}). The different marker types denote different superclusters. The black horizontal line shows a comoving scale of 50 Mpc. Figure A2 shows the optical images of the most massive member clusters of the top five superclusters in Table 2. For more details, see Section 5.1.2.

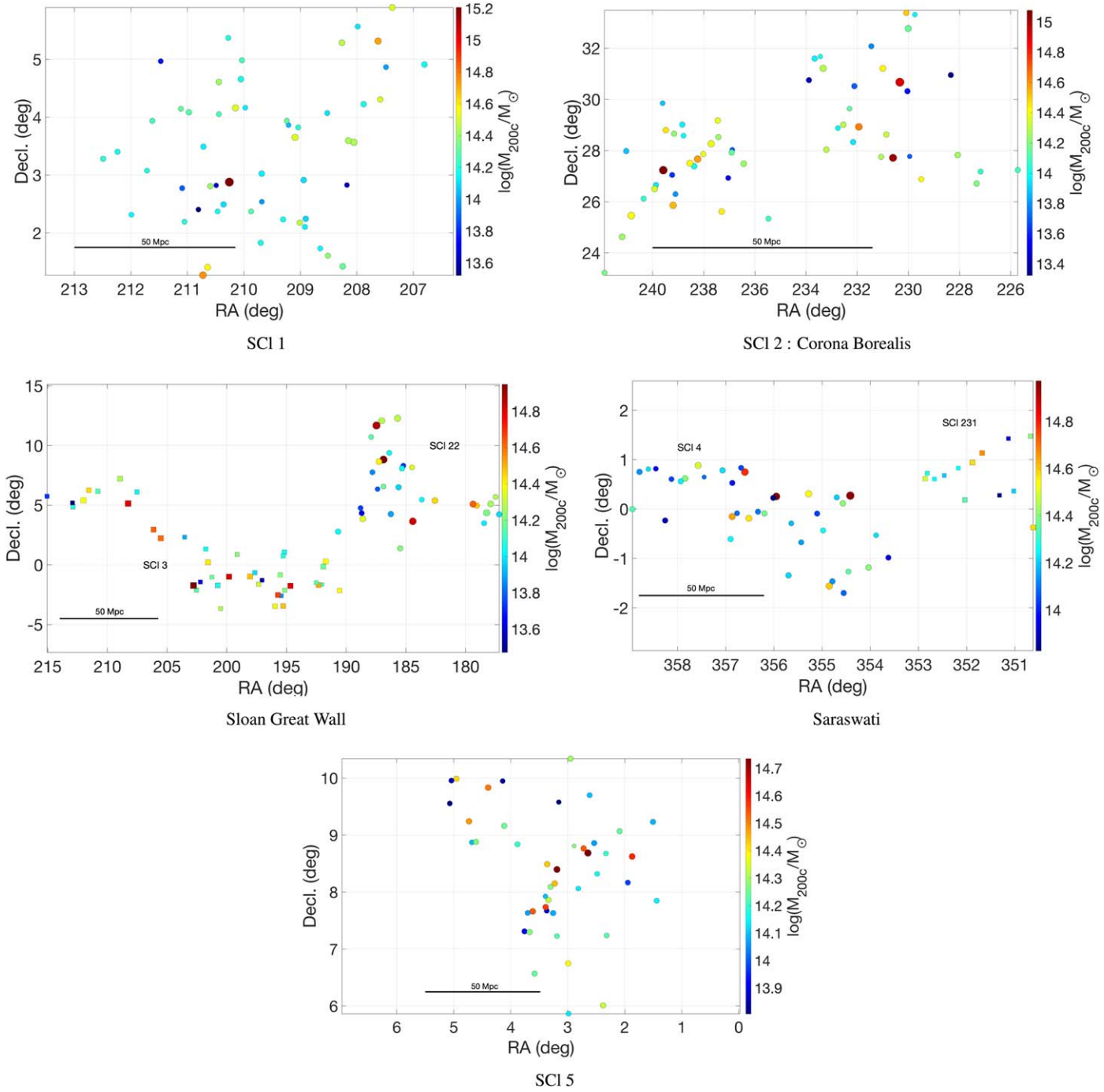

Figure A1. Sky plane distribution of the five most massive superclusters identified in our supercluster catalog.

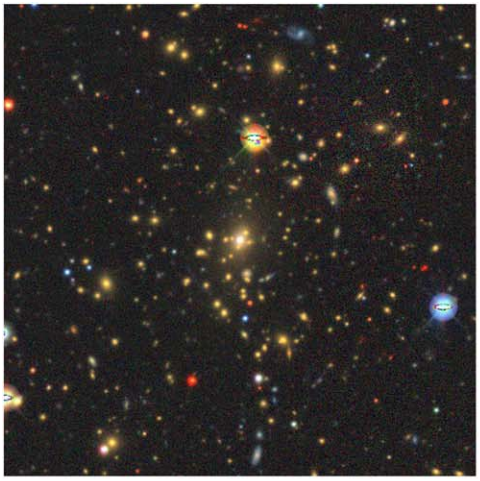

SCl 1 (4′.2 x 4′.2)
Abell 1835 : RA = 210°.25862, Decl. = 2°.87847

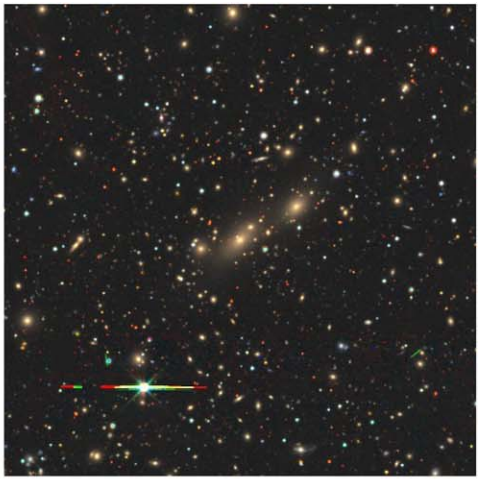

SCl 2 (12′.5 x 12′.5)
Abell 2142 : RA = 239°.58334, Decl. = 27°.23341

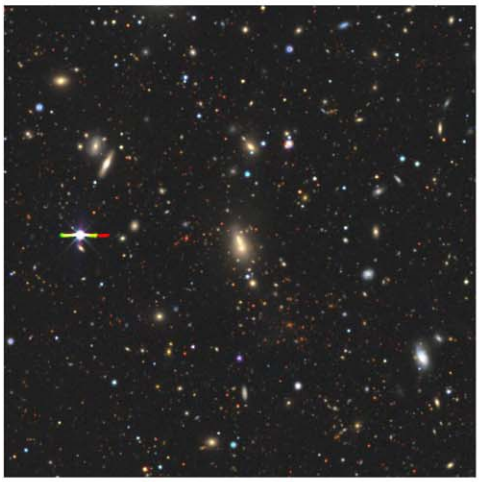

SCl 3 (12′.5 x 12′.5)
Abell 1750N : RA = 202°.79594, Decl. = -1°.72730

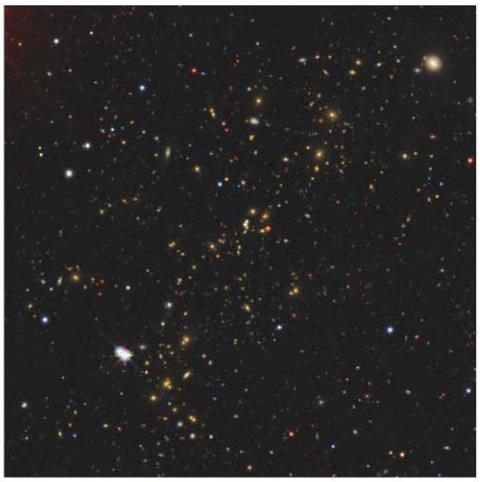

SCl 4 (9′.2 x 9′.2)
ZwCl 2341+0000 : RA = 355°.94806, Decl. = 0°.25666

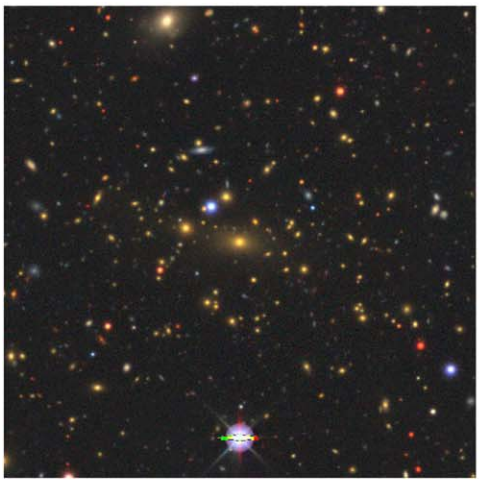

Abell 2631 (4′.2 x 4′.2)
RA = 354°.41554, Decl. = 0°.27137

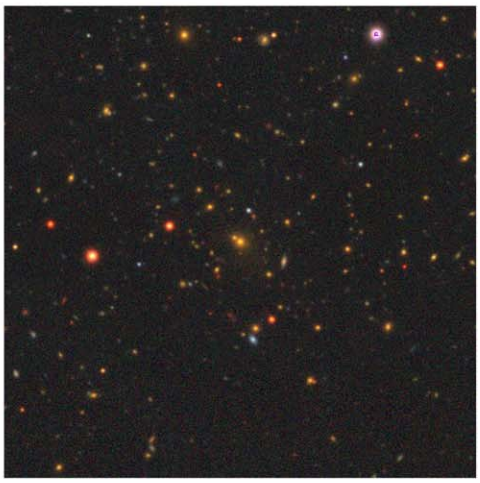

SCl 5 (4′.2 x 4′.2)
RA = 3°.18930, Decl. = 8°.39641

Figure A2. Optical images of the most massive member clusters in each of the top five superclusters in Table 2. Abell 2631 is actually the most massive cluster of SCl 4 (the Saraswati supercluster). The images are extracted from the DESI Legacy Imaging Surveys (DR9).

ORCID iDs

Shishir Sankhyayan https://orcid.org/0000-0003-2601-2707
Joydeep Bagchi https://orcid.org/0000-0002-2922-2884
Elmo Tempel https://orcid.org/0000-0002-5249-7018
Surhud More https://orcid.org/0000-0002-2986-2371
Maret Einasto https://orcid.org/0000-0003-3722-8239
Pratik Dabhade https://orcid.org/0000-0001-9212-3574
Somak Raychaudhury https://orcid.org/0000-0002-4864-4046
Ramana Athreya https://orcid.org/0000-0001-7141-7311
Pekka Heinämäki https://orcid.org/0000-0002-1568-0227

References

Abazajian, K. N., Adelman-McCarthy, J. K., Agüeros, M. A., et al. 2009, ApJS, 182, 543
Abell, G. O. 1958, ApJS, 3, 211
Abell, G. O., Corwin, H. G., Jr., & Olowin, R. P. 1989, ApJS, 70, 1
Alam, S., Albareti, F. D., Allende Prieto, C., et al. 2015, ApJS, 219, 12
Alfaro, I. G., Rodriguez, F., Ruiz, A. N., Luparello, H. E., & Lambas, D. G. 2022, A&A, 665, A44
Araya-Melo, P. A., Reisenegger, A., Meza, A., et al. 2009, MNRAS, 399, 97
Bag, S., Liivamägi, L. J., & Einasto, M. 2023, MNRAS, 521, 4712
Bagchi, J., Durret, F., Neto, G. B. L., & Paul, S. 2006, Sci, 314, 791
Bagchi, J., Enßlin, T. A., Miniati, F., et al. 2002, NewA, 7, 249
Bagchi, J., Sankhyayan, S., Sarkar, P., et al. 2017, ApJ, 844, 25
Barber, C. B., Dobkin, D. P., Dobkin, D. P., & Huhdanpaa, H. 1996, ACM Trans. Math. Softw., 22, 469
Bond, J. R., Kofman, L., & Pogosyan, D. 1996, Natur, 380, 603
Boschin, W., Girardi, M., & Barrena, R. 2013, MNRAS, 434, 772
Busha, M. T., Evrard, A. E., Adams, F. C., & Wechsler, R. H. 2005, MNRAS, 363, L11
Chon, G., Böhringer, H., & Zaroubi, S. 2015, A&A, 575, L14
Chow-Martínez, M., Andernach, H., Caretta, C. A., & Trejo-Alonso, J. J. 2014, MNRAS, 445, 4073
Cucciati, O., Lemaux, B. C., Zamorani, G., et al. 2018, A&A, 619, A49
de Jong, R. S., Agertz, O., Berbel, A. A., et al. 2019, Msngr, 175, 3
Delaunay, B. 1934, Sur la sphére vide, Izvestia Akad Nauk SSSR Otdel. Mat. Sov. Nauk, 7, 793
DESI Collaboration, Aghamousa, A., & Aguilar, J. 2016, arXiv:1611.00036
Dunkley, J., Komatsu, E., Nolta, M. R., et al. 2009, ApJS, 180, 306
Dünner, R., Araya, P. A., Meza, A., & Reisenegger, A. 2006, MNRAS, 366, 803
Dupuy, A., Courtois, H. M., Dupont, F., et al. 2019, MNRAS, 489, L1
Einasto, J., Einasto, M., Tago, E., et al. 2007a, A&A, 462, 811
Einasto, J., Hütsi, G., Saar, E., et al. 2011a, A&A, 531, A75
Einasto, J., Hütsi, G., Suhhonenko, I., Liivamägi, L. J., & Einasto, M. 2021a, A&A, 647, A17
Einasto, J., Klypin, A., Hütsi, G., Liivamägi, L. J., & Einasto, M. 2021b, A&A, 652, A94
Einasto, J., Suhhonenko, I., Liivamägi, L. J., & Einasto, M. 2019, A&A, 623, A97
Einasto, M., Deshev, B., Lietzen, H., et al. 2018, A&A, 610, A82
Einasto, M., Deshev, B., Tenjes, P., et al. 2020, A&A, 641, A172
Einasto, M., Einasto, J., Tago, E., et al. 2007b, A&A, 464, 815
Einasto, M., Gramann, M., Saar, E., et al. 2015, A&A, 580, A69
Einasto, M., Kipper, R., Tenjes, P., et al. 2021c, A&A, 649, A51
Einasto, M., Lietzen, H., Gramann, M., et al. 2016, A&A, 595, A70
Einasto, M., Lietzen, H., Tempel, E., et al. 2014, A&A, 562, A87
Einasto, M., Liivamägi, L. J., Tago, E., et al. 2011b, A&A, 532, A5
Einasto, M., Liivamägi, L. J., Tempel, E., et al. 2011c, ApJ, 736, 51
Einasto, M., Tago, E., Jaaniste, J., Einasto, J., & Andernach, H. 1997, A&AS, 123, 119
Einasto, M., Tago, E., Saar, E., et al. 2010, A&A, 522, A92
Einasto, M., Tenjes, P., Gramann, M., et al. 2022, A&A, 666, A52
Ettori, S., & Balestra, I. 2009, A&A, 496, 343
Frieman, J. A., Turner, M. S., & Huterer, D. 2008, ARA&A, 46, 385
Ghirardini, V., Bulbul, E., Hoang, D. N., et al. 2021, A&A, 647, A4
Górski, K. M., Hivon, E., Banday, A. J., et al. 2005, ApJ, 622, 759
Gott, J. R., III, Jurić, M., Schlegel, D., et al. 2005, ApJ, 624, 463
Heinämäki, P., Teerikorpi, P., Douspis, M., et al. 2022, A&A, 668, A37
Hoffman, Y., Pomarède, D., Tully, R. B., & Courtois, H. M. 2017, NatAs, 1, 0036
Huchra, J. P., & Geller, M. J. 1982, ApJ, 257, 423
Kale, R., Venturi, T., Giacintucci, S., et al. 2015, A&A, 579, A92
Kim, J., Park, C., L'Huillier, B., & Hong, S. E. 2015, JKAS, 48, 213
Kim, J. W., Im, M., Lee, S. K., et al. 2016, ApJL, 821, L10
Knebe, A., Knollmann, S. R., Muldrew, S. I., et al. 2011, MNRAS, 415, 2293
Kolmogorov, A. L. 1933, G. Ist. Ital. Attuari, 4, 83
LaRoque, S. J., Bonamente, M., Carlstrom, J. E., et al. 2006, ApJ, 652, 917
Laureijs, R., Amiaux, J., Arduini, S., et al. 2011, arXiv:1110.3193
Lietzen, H., & Einasto, M. 2016, in IAU Symp. 308, The Zeldovich Universe: Genesis and Growth of the Cosmic Web, ed. R. van de Weygaert et al. (Cambridge: Cambridge Univ. Press), 412
Lietzen, H., Tempel, E., Heinämäki, P., et al. 2012, A&A, 545, A104
Lietzen, H., Tempel, E., Liivamägi, L. J., et al. 2016, A&A, 588, L4
Liivamägi, L. J., Tempel, E., & Saar, E. 2012, A&A, 539, A80
Luparello, H., Lares, M., Lambas, D. G., & Padilla, N. 2011, MNRAS, 415, 964
Martínez, V. J., & Saar, E. 2002, Statistics of the Galaxy Distribution (Boca Raton, FL: Chapman & Hall/CRC)
Monteiro-Oliveira, R., Soja, A. C., Ribeiro, A. L. B., et al. 2021, MNRAS, 501, 756
Nadathur, S., & Crittenden, R. 2016, ApJL, 830, L19
Neyrinck, M. C. 2008, MNRAS, 386, 2101
Parekh, V., Kincaid, R., Thorat, K., et al. 2022, MNRAS, 509, 3086
Park, C., Choi, Y. Y., Kim, J., et al. 2012, ApJL, 759, L7
Pomarède, D., Tully, R. B., Graziani, R., et al. 2020, ApJ, 897, 133
Pomarède, D., Tully, R. B., Hoffman, Y., & Courtois, H. M. 2015, ApJ, 812, 17
Raychaudhury, S. 1989, Natur, 342, 251
Richard, J., Kneib, J. P., Blake, C., et al. 2019, Msngr, 175, 50
Rines, K., & Diaferio, A. 2006, AJ, 132, 1275
Rines, K., Geller, M. J., Diaferio, A., & Kurtz, M. J. 2013, ApJ, 767, 15
Schmidt, R. W., Allen, S. W., & Fabian, A. C. 2001, MNRAS, 327, 1057
Seth, R., & Raychaudhury, S. 2020, MNRAS, 497, 466
Shapley, H. 1930, BHarO, 874, 9
Sheth, R. K., & van de Weygaert, R. 2004, MNRAS, 350, 517
Shimakawa, R., Okabe, N., Shirasaki, M., & Tanaka, M. 2023, MNRAS, 519, L45
Smirnov, N. 1948, Ann. Math. Stat., 19, 279
Suhhonenko, I., Einasto, J., Liivamägi, L. J., et al. 2011, A&A, 531, A149
Teerikorpi, P., Heinämäki, P., Nurmi, P., et al. 2015, A&A, 577, A144
Trayford, J. W., Theuns, T., Bower, R. G., et al. 2015, MNRAS, 452, 2879
Tully, R. B., Courtois, H., Hoffman, Y., & Pomarède, D. 2014, Natur, 513, 71
Tuominen, T., Nevalainen, J., Tempel, E., et al. 2021, A&A, 646, A156
Ueda, S., Kitayama, T., & Dotani, T. 2017, ApJ, 837, 34
van de Weygaert, R. 2016, in IAU Symp. 308, The Zeldovich Universe: Genesis and Growth of the Cosmic Web, ed. R. van de Weygaert et al. (Cambridge: Cambridge Univ. Press), 493
van Weeren, R. J., de Gasperin, F., Akamatsu, H., et al. 2019, SSRv, 215, 16
van Weeren, R. J., Röttgering, H. J. A., Bagchi, J., et al. 2009, A&A, 506, 1083
Venturi, T., Giacintucci, S., Merluzzi, P., et al. 2022, A&A, 660, A81
Wen, Z. L., & Han, J. L. 2015, ApJ, 807, 178
Wen, Z. L., Han, J. L., & Liu, F. S. 2012, ApJS, 199, 34
York, D. G., Adelman, J., Anderson, J. E., Jr., et al. 2000, AJ, 120, 1579